



HAL
open science

Geochronological evidence for continuous exhumation through the ductile-brittle transition along a crustal-scale low-angle normal fault (Simplon Fault Zone, Central Alps)

M. Campani, N. Mancktelow, D. Seward, Yan Rolland, W. Muller, I. Guerra

► **To cite this version:**

M. Campani, N. Mancktelow, D. Seward, Yan Rolland, W. Muller, et al.. Geochronological evidence for continuous exhumation through the ductile-brittle transition along a crustal-scale low-angle normal fault (Simplon Fault Zone, Central Alps). *Tectonics*, 2010, 29, pp.TC3002. 10.1029/2009TC002582 . hal-00498273

HAL Id: hal-00498273

<https://hal.science/hal-00498273>

Submitted on 25 Oct 2021

HAL is a multi-disciplinary open access archive for the deposit and dissemination of scientific research documents, whether they are published or not. The documents may come from teaching and research institutions in France or abroad, or from public or private research centers.

L'archive ouverte pluridisciplinaire **HAL**, est destinée au dépôt et à la diffusion de documents scientifiques de niveau recherche, publiés ou non, émanant des établissements d'enseignement et de recherche français ou étrangers, des laboratoires publics ou privés.

Copyright



Geochronological evidence for continuous exhumation through the ductile-brittle transition along a crustal-scale low-angle normal fault: Simplon Fault Zone, central Alps

M. Campani,^{1,2} N. Mancktelow,¹ D. Seward,¹ Y. Rolland,³ W. Müller,⁴ and I. Guerra⁵

Received 28 July 2009; revised 1 December 2009; accepted 16 December 2009; published 8 May 2010.

[1] Major low-angle normal faults juxtapose different structural levels of the crust that record both brittle and ductile deformation. Field relationships alone cannot establish whether these different responses to deformation represent (1) parts of a single process of exhumation along the detachment or (2) two separate events, with the later, more discrete brittle detachment exhuming a fossil ductile shear zone from depth. These two general models are critically assessed for the low-angle normal Simplon Fault Zone (SFZ) in the central Alps. The SFZ shows a spatial transition from a broad ductile mylonitic shear zone to a discrete brittle detachment with identical kinematics. The age of the ductile shear zone and ductile-brittle transition is controversial. We present a detailed geochronological study based on fission track, ⁴⁰Ar/³⁹Ar, and Rb/Sr microsampling dating, coupled with structural, petrological, and chemical analyses that provides tight constraints on SFZ timing. Discontinuous mineral cooling ages over a broad range of temperatures across the fault zone argue for fault activity between 20 and 3 Ma. On the basis of synkinematic white mica in low-temperature shear zones and necks of foliation boudinage, the brittle-ductile transition in the footwall could be dated at ~14.5–10 Ma. Overall, the data presented here are consistent with a continuous transition from ductile shearing to a more localized zone of brittle deformation within the same geological framework, over a period of ~15 Ma. The SFZ is therefore an example of a telescoped crustal section within a single major low-angle fault, involving a continuous period of exhumation rather than a two-stage structure. **Citation:** Campani, M., N. Mancktelow, D. Seward, Y. Rolland, W. Müller, and I. Guerra (2010), Geochronological evidence for continuous exhumation through the ductile-brittle transition along a crustal-scale low-

angle normal fault: Simplon Fault Zone, central Alps, *Tectonics*, 29, TC3002, doi:10.1029/2009TC002582.

1. Introduction

[2] Major low-angle ($\leq 30^\circ$) normal faults juxtapose different structural levels of the crust, typically across a brittle detachment that overprints an extensional ductile shear zone showing similar kinematics. Many studies imply a model with a single continuous process of exhumation of the footwall along a low-angle detachment that evolves from the ductile to the brittle field [e.g., *Sibson*, 1983; *Mancktelow*, 1985; *Mehl et al.*, 2005]. However, some studies have proposed an alternative model where the mylonites from the footwall are a more general feature of the extending middle crust that are “captured” and exhumed by the late detachment [e.g., *Davis*, 1988; *Lister and Davis*, 1989; *Axen and Bartley*, 1997]. These two general models have different implications in terms of the amount of exhumation involved along a low-angle detachment. In this paper, we investigate these potential models along a well-exposed low-angle detachment in the European Alps, combining detailed geochronology and thermochronology with structural, petrological and chemical analyses. Many studies have already used thermochronology to investigate the timing and rate of exhumation on low-angle detachments [e.g., *Foster et al.*, 1993; *Grasemann and Mancktelow*, 1993; *Wells et al.*, 2000; *Vanderhaeghe et al.*, 2003; *Brichau et al.*, 2006; *Mulch et al.*, 2006], generally based on the concept of cooling ages for different mineral and isotopic systems [e.g., *Wagner et al.*, 1977]. In contrast, absolute ages of deformation are rather difficult to obtain but have been acquired by dating neocrystallized synkinematic minerals (usually white mica) from specific structural sites, such as strain shadows, [*Müller et al.*, 2000a] or from retrograde phyllonitic shear zones [*Dunlap*, 1997; *Challandes et al.*, 2003, 2008; *Kirschner et al.*, 2003; *Mulch and Cosca*, 2004; *Mulch et al.*, 2005; *Rolland et al.*, 2008; *Rolland et al.*, 2009].

[3] The Simplon Fault Zone (SFZ) [*Bearth*, 1956a; *Steck*, 1984, 1987, 1990, 2008; *Mancktelow*, 1985, 1990, 1992; *Merle et al.*, 1986; *Mancel and Merle*, 1987] in the central Alps and the Brenner Fault Zone [*Behrmann*, 1988; *Silverstone*, 1988; *Fügenschuh et al.*, 1997] in the eastern Alps are the most prominent low-angle detachment systems developed in the European Alps. In this paper, we specifically concentrate on the SFZ for several reasons.

1. Overprint of the broad ductile shear zone in the footwall by a more localized brittle detachment can be studied over a strike length of many kilometers.

¹Department of Earth Sciences, ETH Zurich, Zurich, Switzerland.

²Now at Institut für Geologie, Leibniz Universität Hannover, Hannover, Germany.

³Géosciences Azur, Université de Nice Sophia Antipolis, CNRS, IRD, Nice, France.

⁴Department of Earth Sciences, Royal Holloway, University of London, Egham, UK.

⁵IMG, Quartier UNIL-Dorigny, Lausanne, Switzerland.

2. The fault zone exposes different crustal levels, as reflected by the variation in peak metamorphic grade over the region.

3. A large amount of age data (interpreted historically as cooling ages) from the area has already been published [e.g., *Hunziker*, 1969; *Hunziker and Bearth*, 1969; *Purdy and Jäger*, 1976; *Wagner et al.*, 1977; *Deutsch and Steiger*, 1985]. However, interpretations are still controversial mainly because of the lack of structural and petrological constraints on the analyzed samples and the uncertainty as to whether dates were crystallization ages reflecting deformation and mineral growth or cooling ages.

4. The two existing models on the timing of exhumation along low-angle detachments have both been put forward to explain the present features of the SFZ. One model proposes a preceding, early Oligocene ductile shear zone that was subsequently passively exhumed in the late Miocene by a brittle detachment [*Mancel and Merle*, 1987; *Steck*, 1990; *Steck and Hunziker*, 1994]. The alternative model considers the transition from ductile to brittle behavior to be relatively continuous during exhumation in the Miocene [*Mancktelow*, 1985; *Grasemann and Mancktelow*, 1993].

[4] In this paper, we use apatite and zircon fission track ages, $^{40}\text{Ar}/^{39}\text{Ar}$, and Rb/Sr-microsampling dating from synkinematic mica to constrain the timing of the ductile shearing and the transition from ductile to brittle deformation in the SFZ. These geochronological data, in combination with field, microstructural and petrological observations, provide the basis for a critical analysis of the two general models proposed for footwall exhumation along low-angle detachments.

2. Geological Setting

2.1. Simplon Fault Zone

[5] The SFZ (Figure 1) is a major low-angle normal fault that, in its central section, dips 25–30° to the SW. Its exhumed footwall forms the Toce Dome (Figure 1a), which, together with the Ticino Dome further east, comprise the regionally developed Lepontine metamorphic Dome [e.g., *Preiswerk*, 1921; *Wenk*, 1955; *Steck and Hunziker*, 1994]. The immediate footwall of the SFZ is characterized by a transition from a broad ductile mylonitic zone (the “Simplon shear zone”) to a discrete brittle detachment with identical kinematics. The mylonitic zone grades over a distance of 1–2 km into less strongly overprinted units of the Lower Pennine zone [*Milnes*, 1974]. The brittle detachment or “Simplon Line” (SL) [*Mancktelow*, 1985; *Mancel and Merle*, 1987; *Steck*, 1987] consists of a narrow zone (<10 m) of cataclases overprinting the mylonites. In its central section, it is marked by a zone of foliated clay gouge that can be up to a few meters wide. Kinematic indicators from both the ductile and brittle components consistently show a top down to the SW shear sense [*Mancktelow*, 1985, 1987, 1990; *Grosjean et al.*, 2004]. In contrast, older structures are generally well preserved in the hanging wall, showing overprinting relationships between several deformation phases that correspond well in their orientation and style to the four regional phases, D1 to D4 [*Milnes et al.*, 1981]. These ductile structures are nonpervasively overprinted by brittle faults. The older

regionally developed fold structures and foliations [e.g., *Steck and Hunziker*, 1994; *Grujic and Mancktelow*, 1996; *Maxelon and Mancktelow*, 2005] are also observed in the footwall but are overprinted and transposed by the Simplon shear zone close to the detachment.

2.2. Metamorphic History

[6] In the central Alps, some nappes display evidence of an early high- to locally ultrahigh-pressure Alpine metamorphic event [e.g., *Lardeaux et al.*, 1982; *Chopin and Monié*, 1984; *Heinrich*, 1986; *Reinecke*, 1991; *Bousquet et al.*, 2008; *Wiederkehr et al.*, 2008]. A subsequent regional, temperature-dominated Barrovian metamorphism overprints and crosscuts nappe boundaries (Figure 1a). The grade of this regional metamorphism increases systematically toward the internal regions, from middle greenschist facies in the NW (Rhône Valley) to middle amphibolite facies in the SE (Ossola Valley) [*Bearth*, 1958; *Niggli and Niggli*, 1965; *Trommsdorff*, 1972; *Wenk and Wenk*, 1984]. In the Upper Pennine zone (SW of the SL [*Milnes*, 1974]), maximum metamorphic conditions attain ~620–700°C and 0.5 GPa in the deepest Camughera-Moncuoco unit toward the south [*Keller et al.*, 2005a]. In the Lower Pennine zone (i.e., NE of the SL), the Alpine metamorphism in the Mesozoic cover has been studied in detail by *Frank* [1983]. His geothermobarometric analysis showed a systematic increase in grade from middle greenschist (400–420°C, 0.2–0.3 GPa) to middle amphibolite facies (580–620°C, 0.6–0.8 GPa) from the NW to the SE. *Vance and O’Nions* [1992] dated the climax of this metamorphism, using U/Pb and Rb/Sr methods on garnet from the Mesozoic cover near the staurolite isograd in the Toce Dome (i.e., in the footwall of the SFZ). They obtained an age of circa 30 Ma, with garnet growth requiring a time interval of 2.9 ± 1.5 Ma. The pattern of isograds and mineral zone boundaries has been extensively described in the literature [e.g., *Trommsdorff*, 1966; *Frey et al.*, 1974; *Steck and Hunziker*, 1994; *Frey and Ferreiro Mählmann*, 1999; *Engi et al.*, 2004; *Bousquet et al.*, 2008]. The SFZ offsets these isograds (Figure 1a) and a clear jump in metamorphic grade can be observed in the central region, from greenschist facies in the hanging wall to amphibolite facies in the footwall. Ductile shearing in the footwall of the SFZ clearly postdates the peak of metamorphism and was responsible for the exhumation and associated cooling of the footwall [e.g., *Hunziker and Bearth*, 1969; *Mancktelow*, 1985; *Merle et al.*, 1986].

2.3. Previous Thermochronological and Geochronological Work

[7] The central Alps were a very important region for the development of thermochronology and it was here that the concept of a “blocking temperature” for a specific mineral and isotopic system was first introduced [*Jäger*, 1965; *Jäger et al.*, 1967]. This concept was later extended by *Dodson* [1973] to the notion of a “closure temperature,” including the influence of cooling rates and grain size. The pioneering work of *Jäger* and coworkers [*Jäger*, 1965; *Armstrong et al.*, 1966; *Jäger et al.*, 1967] suggested that blocking of the K/Ar and Rb/Sr systems in biotite occurred during post-

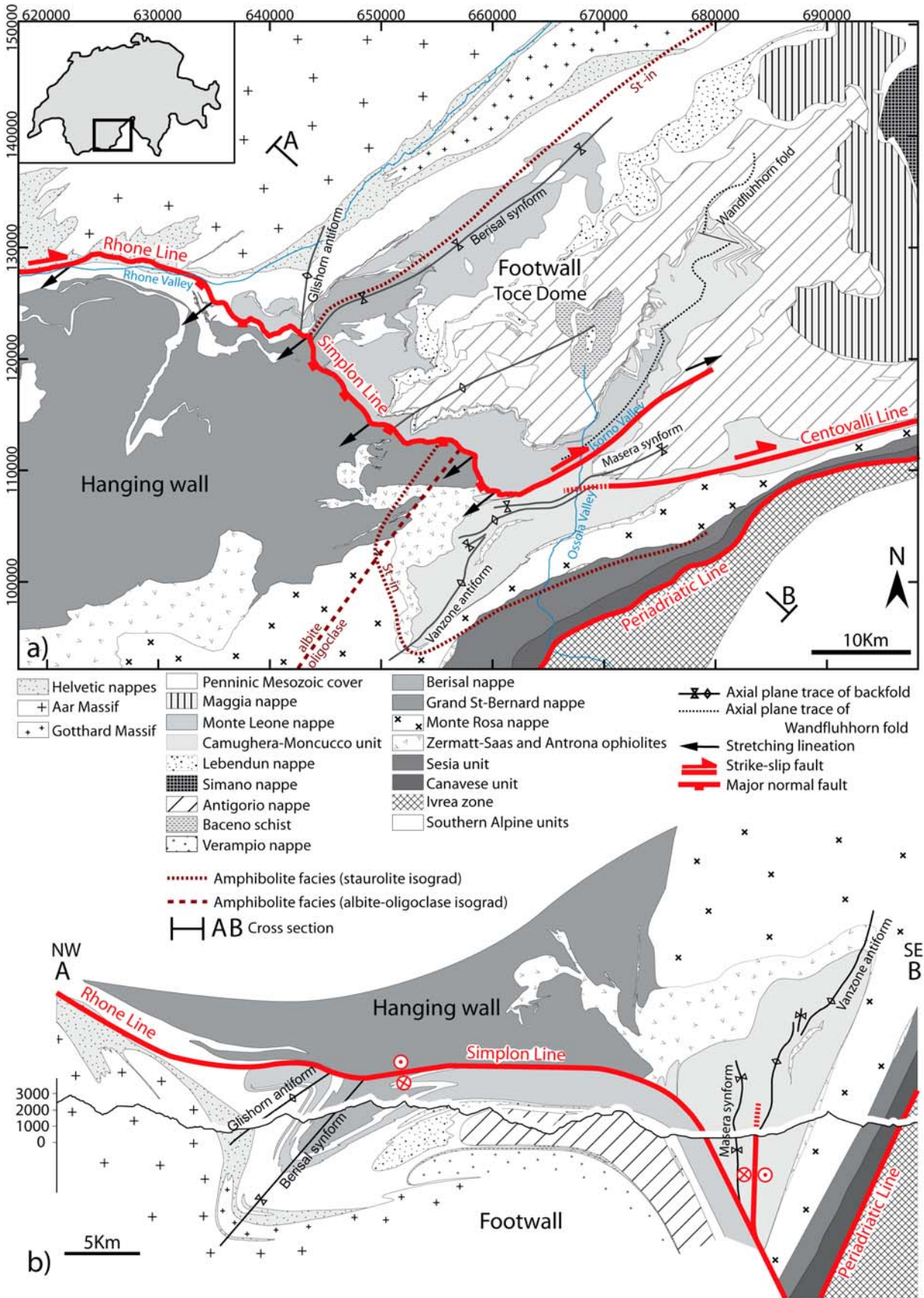


Figure 1

metamorphic cooling, following isotopic resetting around the peak of Alpine metamorphism. Since then, many geochronological studies have been carried out in the central Alps and a large number of radiometric ages were published: fission track ages on apatite and zircon, K/Ar and $^{40}\text{Ar}/^{39}\text{Ar}$ ages on white mica and biotite, and Rb/Sr isotope ages on white mica and biotite [e.g., Hunziker, 1969; Hunziker and Bearth, 1969; Purdy and Jäger, 1976; Wagner *et al.*, 1977; Frank and Stettler, 1979; Deutsch and Steiger, 1985; Michalski and Soom, 1990; Soom, 1990]. All these ages have been interpreted as cooling ages. A detailed study on biotite $^{40}\text{Ar}/^{39}\text{Ar}$ cooling ages, carried out by Baxter *et al.* [2002] at the contact between metapelite and amphibolite units in the central region of the SFZ, has shown a correlation of excess argon with lithology. These authors suggest that $^{40}\text{Ar}/^{39}\text{Ar}$ cooling ages should be determined on several samples from each outcrop to avoid errors introduced by local excess argon.

[8] The work of Hunziker and Bearth [1969] was the first to establish a marked change in biotite Rb/Sr ages across the SFZ, indicating a major normal component in the central region, with a younger age (11 Ma) in the footwall compared to the hanging wall (15–22 Ma). Further studies have confirmed this thermochronological jump in cooling ages for a range of minerals and isotopic systems (see synthesis in Steck and Hunziker [1994]). There is a consistent jump between older ages in the hanging wall (from circa 35 Ma with muscovite Rb/Sr to circa 5 Ma with apatite fission track) to younger ages in the footwall (from circa 20 Ma with muscovite Rb/Sr to circa 3 Ma with apatite fission track). Most recently, in the southern and southeastern continuation of the SFZ across the Ossola valley, Keller *et al.* [2005b] have shown that there is no jump recorded in the fission track ages for zircon and apatite. Instead there is a progressive and gradual decrease in age to the north across the SFZ (from 12 Ma to 5.4 Ma with zircon and from 5.8 Ma to 2.2 Ma with apatite). In the northwestern part, across the Rhone Valley (Figure 1a), a clear jump in cooling ages is shown by the fission track ages [Soom, 1990; Seward and Mancktelow, 1994; Vernon *et al.*, 2008]. Nevertheless, almost no radiometric ages were previously available between the Rhone Valley and the central region of the SFZ and a continuation of the thermochronological jump into the Rhone Valley was not well established.

[9] According to Steck and Hunziker [1994], the development of the Glishorn and Berisal back folds in the northern part of the footwall (Figure 1b) was associated with the young exhumation of the Aar Massif in the late Miocene, as established from fission track cooling ages [e.g., Michalski and Soom, 1990]. In turn, the brittle detachment (SL) was also considered to be late Miocene because it crosscuts these back folds (Figure 1b). Based on the available data, two different models had been proposed for the age of the SFZ.

One model proposes the lower Oligocene development of a broad extensional ductile shear zone that is not only restricted to the footwall but also covers a wide zone within the hanging wall [Merle, 1987; Steck and Hunziker, 1994]. The intrusion age (from zircon U/Pb) of 29 to 26 Ma for synkinematic to postkinematic pegmatites within the interpreted prolongation of this major shear zone in the steep zone north of the Periadriatic Line provides a minimum age for this shearing event [Romer *et al.*, 1996]. However, as noted above, the thermochronological jump and crosscutting relationship of the back folding in the footwall demonstrates Neogene activity on the brittle SL detachment. In this model, the brittle detachment is therefore considered to be a late Miocene structure that captures and exhumes the largely Oligocene “fossil” shear zone. The alternative model considers the current geometry to reflect the more-or-less continuous development during the Miocene of a major low-angle fault zone that evolves from a broad ductile shear zone to a more discrete brittle detachment as the footwall exhumes and cools [Mancktelow, 1985, 1990, 1992]. In this second model, the ductile shear zone directly related to this fault zone development is restricted to the footwall, with the mylonites present in the hanging wall corresponding to an older (and indeed probably Oligocene) structure. Based on this more continuous concept, Grasemann and Mancktelow [1993] developed a two-dimensional thermal model using published isotopic mineral cooling ages. They concluded that the most active period for the SFZ was between 18 Ma and 15 Ma, but with a continuation until at least 5 Ma.

[10] Subsequently, illite from clay-gouge marking the brittle detachment in the central region has been dated by K/Ar methods at circa 5–7 Ma [Zwingmann and Mancktelow, 2004]. Muscovite from a mesothermal gold vein located in the footwall of the SFZ in the central region was dated using $^{40}\text{Ar}/^{39}\text{Ar}$ by Pettke *et al.* [1999]. These veins occur in extensional faults and fractures that crosscut the greenschist to amphibolite facies metamorphic fabric of the wall rock. The muscovite gives ages of 11.6 ± 0.1 Ma for veins crosscutting the mylonites of the SFZ and 10.6 ± 0.3 Ma further east within the core of the Toce Dome. These ages were interpreted as crystallization ages, as they yield younger ages than the metamorphic muscovite in the immediately adjacent host rock. These ages therefore date brittle fracturing occurring between 11.6 and 10.6 Ma. The age range is consistent with the recent work of Hetherington and Villa [2007], who dated brittle fracturing and multistage vein filling in the footwall Berisal unit (Figure 1) using $^{40}\text{Ar}/^{39}\text{Ar}$ on muscovite, with ages ranging from 6 to 11 Ma. K/Ar ages reported by Purdy and Stalder [1973] on muscovite and biotite in late veins from the Simplon rail tunnel cover the range circa 10–14 Ma and also provide constraints on the timing of late fracturing in the footwall of the SFZ.

Figure 1. Geological setting of the Simplon Fault Zone in the central Alps. (a) Geological map summarizing our own field observations and those compiled from the published geological maps of Raron, Brig, Simplon, Domodossola, and Keller *et al.* [2005b]. The greenschist/amphibolite facies boundary is drawn based on the staurolite isograd (St-in) of Niggli [1970] to the NE of the Simplon Line and on the albite-oligoclase isograd [Bearth, 1958] and the staurolite isograd [Keller *et al.*, 2005a] to the SW of the Simplon Line. (b) NW-SE cross section perpendicular to the regional fold axes and stretching lineation and thus perpendicular to the orogen-parallel movement on the SFZ.

[11] In summary, it is well accepted that the brittle detachment (SL) was active during the late Miocene. However, the absolute age of the broad ductile shear zone in the footwall and the time of transition to brittle deformation are still controversial. The age of mylonitic fabrics older than the Simplon mylonites in footwall and hanging wall is relevant for distinguishing between the two proposed models. *Markley et al.* [1998] used $^{40}\text{Ar}/^{39}\text{Ar}$ geochronology to date synkinematic white mica from a greenschist facies mylonite related to the emplacement of the Siviez-Mischabel nappe in the hanging wall of the SFZ, at about 41–36 Ma. They noted that fine-grained white micas (20 μm) from the hanging wall close to the SL detachment were partially reset at 22 Ma. They suggested that thermal reset was most likely due to increasing temperature caused by footwall exhumation, or to Oligocene magmatic activity in the lower Pennine nappes. *Hetherington and Villa* [2007] obtained $^{40}\text{Ar}/^{39}\text{Ar}$ ages of around 17 Ma for muscovite defining the main foliation in the Berisal Unit from the SFZ footwall. They considered this to date the regional (S_2) main foliation [e.g., *Grujic and Mancktelow*, 1996; *Maxelon and Mancktelow*, 2005] and thus to represent a maximum age for the onset of the Simplon shear zone, which overprints and transposes S_2 . In the Helvetic nappes north of the Rhone Valley and in the interpreted prolongation of the SFZ footwall, *Kirschner et al.* [2003] also applied $^{40}\text{Ar}/^{39}\text{Ar}$ and Rb/Sr methods to directly date synkinematic white micas related to nappe thrusting and established that activity or reactivation lasted until 25–15 Ma. They proposed that the Rhone (Simplon) Line (Figure 1), which crosscuts the “root” of the Helvetic nappes, was therefore active at around 17 Ma, which is close to the 19 Ma age proposed for movement on the same structure by *Markley et al.* [1998].

3. Field Observations

[12] The SFZ is structurally and geomorphologically well-defined in its central part (region I in Figure 2a), with a corresponding marked jump in both metamorphic grade and geochronologic ages. However, its prolongation further to the NW and SE is controversial. We carried out a detailed structural analysis (Figure 2) to establish the possible continuation of the SFZ in these regions and to determine how displacement on this major fault zone was either accommodated or transferred.

3.1. SE Prolongation of the Simplon Fault Zone

[13] In regions II and III (Figure 2a), clear structural and geomorphological evidence for the SFZ is missing: the strike of foliation is effectively parallel in the footwall and hanging wall, there is no clear difference in metamorphic grade, and apatite and zircon fission track ages across this section do not show any significant jump in central ages [*Keller et al.*, 2005b]. As a result, the continuation of the SFZ to the SE was still controversial and different models have been proposed: (1) a continuation of the brittle SL into the E-W striking Centovalli Line (Figure 1a), where clear brittle deformation was described [e.g., *Bearth*, 1956b; *Laubscher*, 1971; *Schmid and Kissling*, 2000; *Steck*, 2008]; (2) a continuation of the SFZ (both ductile shearing and the

brittle detachment) across the Ossola Valley into the Isorno Valley toward the NE (Figure 1a) and into the Toce Dome [*Mancktelow*, 1985, 1990, 1992]; and (3) no prolongation at all of the SFZ in the SE region but rather an accommodation by back folding (Masera and Vanzone folds) associated with anticlockwise rotation of the hanging wall [*Keller et al.*, 2006].

[14] In the SE region (i.e., regions II and III, Figure 2a), the Monte Leone unit (Figure 1) shows a strong penetrative mylonitic foliation (Figure 2b, regions II and III) with well developed and unequivocal shear criteria indicating a dextral sense (e.g., sheared and boudinaged quartz veins rotated into the foliation plane (Figure 3a) and shear band or C' structures [*Berthé et al.*, 1979]). In region II, the foliation strike has an E-W orientation and swings into a WSW-ENE orientation in region III (Figure 2b), where the foliation dips steeply to the SSE ($\sim 60^\circ$ toward 155° , Figure 2c) and forms part of the Southern Steep Belt [*Milnes*, 1974]. The stretching lineation plunges SW in region II and ENE in region III (Figure 2c), with a broad transition where the lineation is close to horizontal. This gradual change in plunge of the stretching lineation defines an overall domal shape [*Mancktelow*, 1985]. The penetrative mylonitic overprint in the Monte Leone unit (regions II and III) is gradual over 100–200 m. To the north, parasitic F_2 folds (related to D2 deformation phase [e.g., *Milnes et al.*, 1981]) are recognized. The mylonitic foliation seems to be axial plane of these F_2 fold structures and therefore would correspond to an S_2 fabric. However, the current study also establishes that the mylonitic foliation crosscuts the SE limb of the Wandfluhhorn fold (Figure 2b), which was interpreted by *Maxelon and Mancktelow* [2005] to be a regional F_2 structure. Therefore, at least for this region, S_2 and the Simplon mylonitic foliation (S_m) are clearly distinct (Figure 2b) and cannot correspond to the same structural event. Further to the NE (region III, Figure 2a), the penetrative mylonitic overprint progressively diminishes and dextral shearing eventually can no longer be distinguished. In this region, there is no evidence for a continuation of a penetrative mylonitic fabric.

[15] In region III, veins rich in quartz, calcite and white mica can be found in a range of different lithologies (Figure 3b). These veins vary in their geometry relative to the mylonitic foliation (Figure 3c). Some veins are little deformed and are oriented perpendicular to the stretching lineation and at a high angle to the foliation. Such veins either have an oblique Riedel shear geometry, consistent with bulk dextral shear, or an extensional geometry related to foliation boudinage [e.g., *Lacassin*, 1988; *Arslan et al.*, 2008]. Others make a smaller angle to the foliation and show evidence of flanking structure [e.g., *Passchier*, 2001] development related to dextral rotation, whereas some are more strongly sheared (in a dextral sense), boudinaged, and now effectively parallel to the foliation. We interpret these structures as an expression of the ductile-brittle transition in this region, with the progressive development of fractures (veins) during continued dextral shearing (Figure 3c). Subsequent fully brittle deformation is seen as localized cataclastic zones and discrete brittle fractures with a clear dextral strike slip sense (Figure 3d). Chloritic alteration on the foliation planes (Figure 3e) with a nearly horizontal striation plunging $0\text{--}6^\circ$ toward 060°

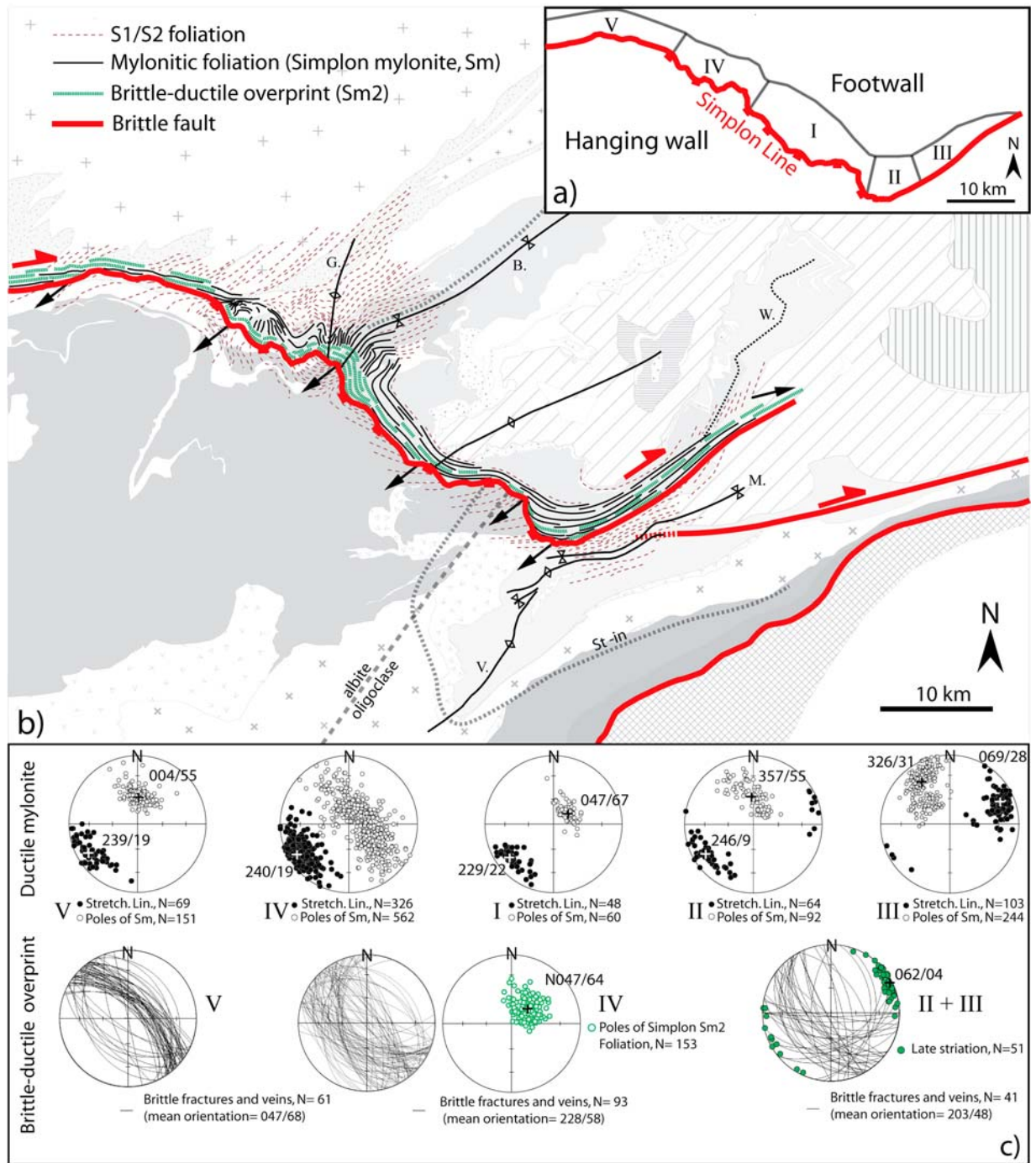


Figure 2. (a) Subdivision into geographical regions I to V. (b) Structural map of the Simplon Fault Zone; the legend is given in Figure 1. G., Glishorn antiform; B., Berisal synform; M., Masera synform; V., Vanzone antiform; W., Wandfluhhorn fold axial plane. (c) Stereoplots of field measurements from the different regions; lower hemisphere, equal-area projection, mean values for lineation and pole to foliation.

(Figure 2c) is also common. Chlorite-bearing slickenfibers show steps indicating brittle dextral strike-slip motion. In the NE of region III, the ductile dextral shearing diminishes and the late brittle overprint becomes more dominant. The domal shape described by the opposite plunge of the

stretching lineations in the ductile mylonitic foliation is not seen in the latest brittle history, and the brittle striation is always nearly horizontal.

[16] As outlined above, the mylonitic foliation in the footwall of the SFZ and the ductile to brittle overprint

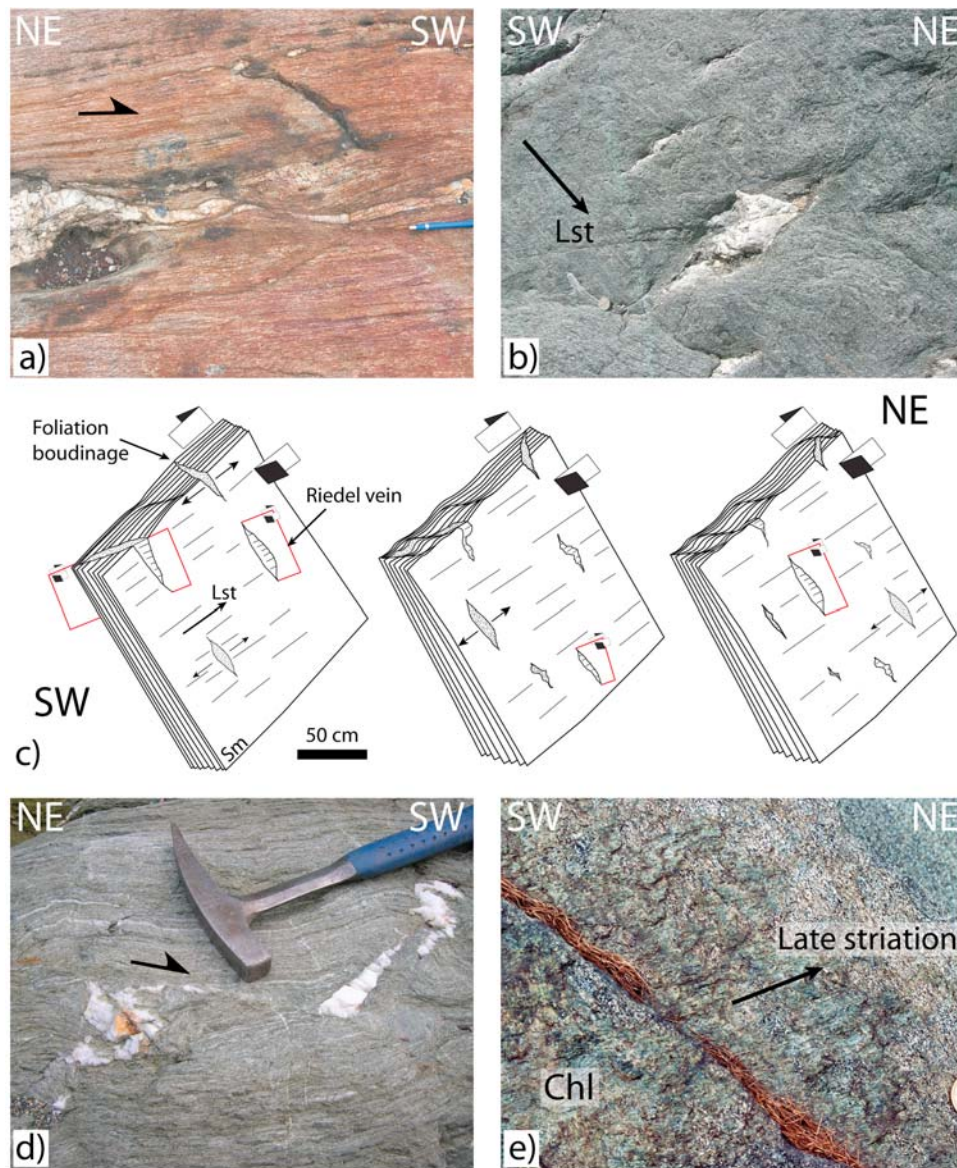


Figure 3. Field observations from the SE regions II and III. (a) Boudinaged quartz vein affected by dextral shearing in the Simplon mylonites, region III (668371/112282). (b) Quartz-muscovite-calcite rich veins formed in the necks of foliation boudinage within the Simplon mylonites, region III (671041/113156). (c) Synthetic sketch representing the successive development and deformation of the quartz-muscovite-calcite rich veins during ongoing shearing, region III. (d) Brittle dextral strike slip fracture, region II (661997/108029). (e) Late chlorite overprint with horizontal striation, region III (676332/117670).

marking the boundary between footwall and hanging wall (i.e., the Simplon Line) can be followed continuously along strike from region I to II and, with a gap marked by the broad Ossola Valley, into region III (Figures 1 and 2). In region III, crosscutting relationships demonstrate that these SFZ-related fabrics are younger than the regional S_2 foliation, whereas in regions I and II the broad mylonitic zone in the SFZ footwall overprints and transposes the S_2 into effective parallelism (Figure 2b).

[17] Many authors have proposed or implied a connection of the SFZ or at least the more brittle Simplon Line with the

steep, brittle, dextral strike-slip Centovalli Line [e.g., Laubscher, 1971, Figure 1; Schmid *et al.*, 2004, Figure 1; Vernon *et al.*, 2008, Figure 2; Steck, 2008, Figure 1]. In the hanging wall of regions II and III, an open synform (Masera synform) and a tighter antiform are mapped on both sides of the Ossola Valley [Milnes *et al.*, 1981, Figure 2; Mancktelow, 1985; Keller *et al.*, 2005b, Figure 2; Keller *et al.*, 2006, Figure 2; Steck, 2008, Figure 3] (compare Figure 2b). Any connection of the Centovalli and Simplon lines must crosscut the hinges of these folds but there is no discernible offset (Figure 2b). The width of alluvial cover in the Ossola

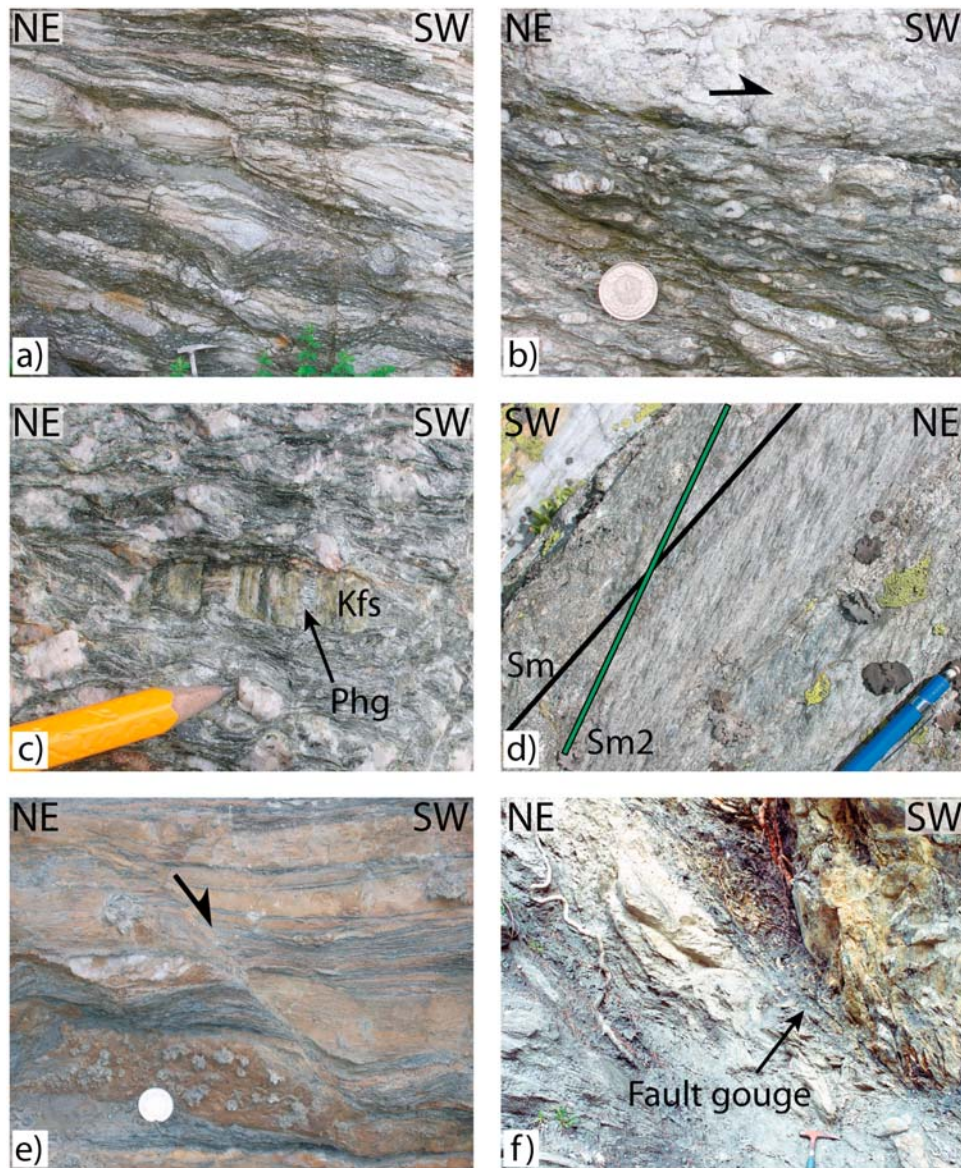


Figure 4. Field observations from the NW region (region V). (a) Boudinaged foliated phyllonite developed from orthogneiss of the Aar massif, region V (633223/128447). (b) Foliated phyllonite with top-to-SW shear band development, region V (633223/128447). (c) Stretched feldspar porphyroclast with synkinematic fibrous phengite, region V (634791/129330). (d) Greenschist facies mylonite (Sm2) transecting the ductile Simplon mylonites (Sm), region IV (644271/121281). (e) Ductile-brittle shear band with sense of shear top to the SW, region IV (630943/127014). (f) Fault gouge, region IV (634954/125166).

Valley allows some degree of freedom in interpretation, but the horizontal displacement involved along any possible connection of the Centovalli and Simplon lines cannot be greater than a few hundred meters.

3.2. NW Prolongation of the Simplon Fault Zone

[18] In the Rhone Valley (region V, Figure 2a), the moderately to steeply SE dipping “roots” of the Helvetic nappes are crosscut by a dextral shear zone with identical

kinematics to the SFZ [Steck, 1984; Burkhard, 1988]. These previous studies proposed a connection of the Simplon Line (SL) with the Rhone Line, with the composite structure referred to as the Rhone-Simplon Line.

[19] In the Rhone Valley (region V), orthogneiss of the Aar massif and its Mesozoic cover are overprinted by a 1–1.5 km wide zone of foliated phyllonites (Figure 4a). Kinematic indicators show a strong dextral component of shear (Figure 4b) and a strong stretching component (Figure 4c) with a stretching lineation plunging around

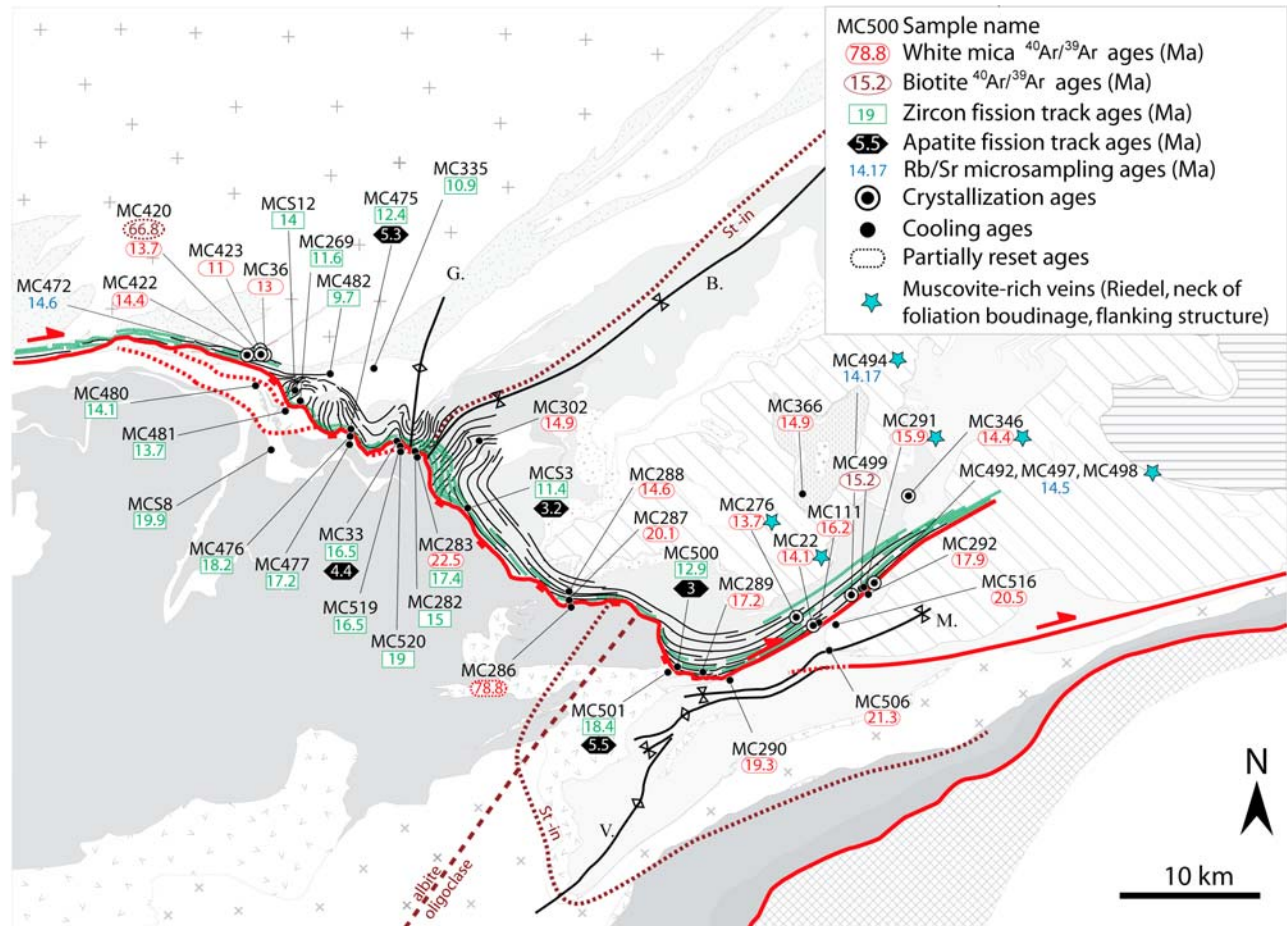


Figure 5. Geochronological map and sample locations; legend is given in Figure 1. G., Glishorn antiform; B., Berisal synform; M., Masera synform; V., Vanzone antiform.

20° toward 240° (Figure 2c). In these phyllonites, fluid infiltration has been important and pervasive, as shown by the transformation of feldspar to white mica, the ubiquitous presence of calcite-rich veins, and sparsely distributed calcite and pyrite within the phyllonitized orthogneissic host rock.

[20] In the adjacent region IV, the 3D geometry is quite complex, there is no longer a clear structural discontinuity between footwall and hanging wall, and the metamorphic grade to either side is similar. In this region, the Simplon mylonitic foliation, Sm, is folded around the Glishorn and Berisal back folds [Steck, 1984; Mancktelow, 1990, 1992] (Figure 2b). The stretching lineation is parallel to the fold axes and consistently plunges around 20° toward 240° (Figure 2c), which is identical to its orientation in region V. The brittle detachment fault crosscuts the folded mylonitic foliation, Sm. A narrow band of greenschist facies mylonites (with foliation Sm2), of ~100 m width, is concordant with the brittle detachment, and transects the main folded foliation Sm (Figure 4d) [Mancktelow, 1992; Mancktelow and Pavlis, 1994]. In this region IV, the ductile-to-brittle and brittle overprints are not strongly localized but instead distributed over several kilometers (Figure 2b). Ductile-brittle shear bands with top-to-SW sense of shear are observed

within both the footwall and hanging wall (Figure 4e). A strong subsequent brittle overprint, with cataclasite, gouge (Figure 4f) and discrete fractures carrying slickenfibers of calcite, also has a sense of displacement top-to-SW.

[21] In summary, going from the SE (region III) to the NW (region V), the metamorphic grade decreases and the deformation associated with the SFZ becomes less localized. Over the whole strike length of the fault zone, ductile and brittle deformation are clearly interrelated, with an apparently continuous transition from ductile, to mixed brittle-ductile, to brittle behavior, while maintaining identical kinematics. Stretching lineations and striations have the same orientation, with a constant SW-NE extension direction throughout. The only exception is in the SE (regions II and III), where the earlier ductile and brittle-ductile stretching direction outlines a broad dome, whereas the later striae maintain a relatively constant and near horizontal direction.

4. Methods and Sample Description

[22] Sample locations are shown on Figure 5, and the corresponding Swiss topographic map grid coordinates are listed in Table 1.

Table 1. Sample Descriptions and Locations^a

Metamorphic Grade	Deformation Phase	Sample	Location	Elevation (m)	Unit	Rock Type	Mica Structure	Method
Greenschist facies	Sm mylonite	MC36	633142/128177	656	Aar Massif	<i>Footwall</i> phyllonite phyllonite phyllonite phyllonite calcschist orthogneiss sandstone orthogneiss quartzite quartzite micashist orthogneiss orthogneiss calcschist fine-grained orthogneiss fine-grained orthogneiss fine-grained orthogneiss fine-grained orthogneiss vein vein vein vein vein vein vein metapelite	thin synkinematic Phg in Sm	⁴⁰ Ar/ ³⁹ Ar
		MC420	633077/128267	670	Aar Massif		synkinematic Phg in Sm and deformed Bt porphy.	⁴⁰ Ar/ ³⁹ Ar
		MC422	632908/128354	661	Aar Massif		thin synkinematic Phg in Sm	⁴⁰ Ar/ ³⁹ Ar
		MC423	633131/128697	658	Helvetic nappes		thin synkinematic Phg in Sm	⁴⁰ Ar/ ³⁹ Ar
		MC472	638903/123565	1072	Aar Massif		thin Phg fiber between stretched Kfs	Rb/Sr
		MCS12	634585/125889	756	Penninic M. cover			fission track
		MC33	641877/123039	2606	Monte Leone			fission track
		MC269	635324/125316	1029	Penninic M. cover			fission track
		MC475	638903/123565	2273	Monte Leone			fission track
		MC335	640487/127471	1181	Penninic M. cover			fission track
		MC482	637778/127174	830	Penninic M. cover			fission track
		MC302	647034/122940	1960	Berisal			⁴⁰ Ar/ ³⁹ Ar
		MCS3	646249/118442	1641	Monte Leone			fission track
		MC287	652595/112713	1406	Monte Leone			⁴⁰ Ar/ ³⁹ Ar
		MC288	652728/113378	1277	Penninic M. cover			⁴⁰ Ar/ ³⁹ Ar
		MC500	659449/108512	852	Monte Leone			fission track
		MC289	660891/108102	655	Monte Leone			⁴⁰ Ar/ ³⁹ Ar
		MC111	668515/114408	422	Monte Leone			⁴⁰ Ar/ ³⁹ Ar
		MC499	671101/113266	710	Monte Leone			⁴⁰ Ar/ ³⁹ Ar
		MC22	668302/11332	397	Monte Leone			⁴⁰ Ar/ ³⁹ Ar
MC276	666833/112119	419	Monte Leone		⁴⁰ Ar/ ³⁹ Ar			
MC346	674157/119606	1406	Monte Leone		⁴⁰ Ar/ ³⁹ Ar			
MC492	-	-	Monte Leone		Rb/Sr			
MC494	671080/113234	692	Monte Leone		Rb/Sr and oxygen isotope			
MC497	-	-	Monte Leone		Rb/Sr and oxygen isotope			
MC498	-	-	Monte Leone		oxygen isotope			
MC291	671100/113274	710	Monte Leone		⁴⁰ Ar/ ³⁹ Ar			
MC366	667203/119928	693	Baceno schist		⁴⁰ Ar/ ³⁹ Ar			
Greenschist facies	S1/2	MC480	633106/126381	1152	Penninic M. cover	<i>Hanging Wall</i> quartzite paragneiss calcschist quartzite paragneiss quartzite paragneiss quartzite quartzite paragneiss paragneiss orthogneiss paragneiss paragneiss Camug.-Monc. Camug.-Monc. Camug.-Monc. Camug.-Monc.	crenulated Ms in S1 and annealed Ms in S2	⁴⁰ Ar/ ³⁹ Ar and fission track
		MC481	634746/124983	902	Grand St Bernard		annealed mica in S1/2	⁴⁰ Ar/ ³⁹ Ar
		MCS8	633787/122299	703	Penninic M. cover		annealed mica in S1/2	fission track
		MC476	638814/123323	2224	Penninic M. cover		annealed in S1/2	fission track
		MC477	638758/122551	2204	Grand St Bernard		annealed in S1/2	fission track
		MC519	641933/122507	2579	Penninic M. cover		annealed in S1/2	fission track
		MC520	642035/122277	2608	Grand St Bernard			fission track
		MC282	642919/122156	2357	Penninic M. cover			fission track
		MC283	642976/122003	2357	Grand St Bernard			fission track
		MC286	652720/112592	1480	Grand St Bernard			fission track
		MC501	659008/108149	868	Camug.-Monc.			fission track
		MC290	662971/108054	504	Camug.-Monc.			fission track
		MC292	671063/113076	544	Camug.-Monc.			fission track
		MC506	668781/109542	310	Camug.-Monc.			fission track
MC516	669466/111221	631	Camug.-Monc.		fission track			

^aLocations are given in Swiss map coordinates. Mineral abbreviations are taken from *Kretz* [1983]. Mica structures are only given for methods where mica was actually analyzed (⁴⁰Ar/³⁹Ar, Rb/Sr and oxygen stable isotopes). Sm, Simpon mylonites; S1/2, foliation related to the D1 and D2 deformation phases [Milnes *et al.*, 1981]; Penninic M. cover, Penninic Mesozoic cover; Camug.-Monc., Camughera-Monucco unit. MC492, MC497, and MC498 come from boulders in the Isorno River.

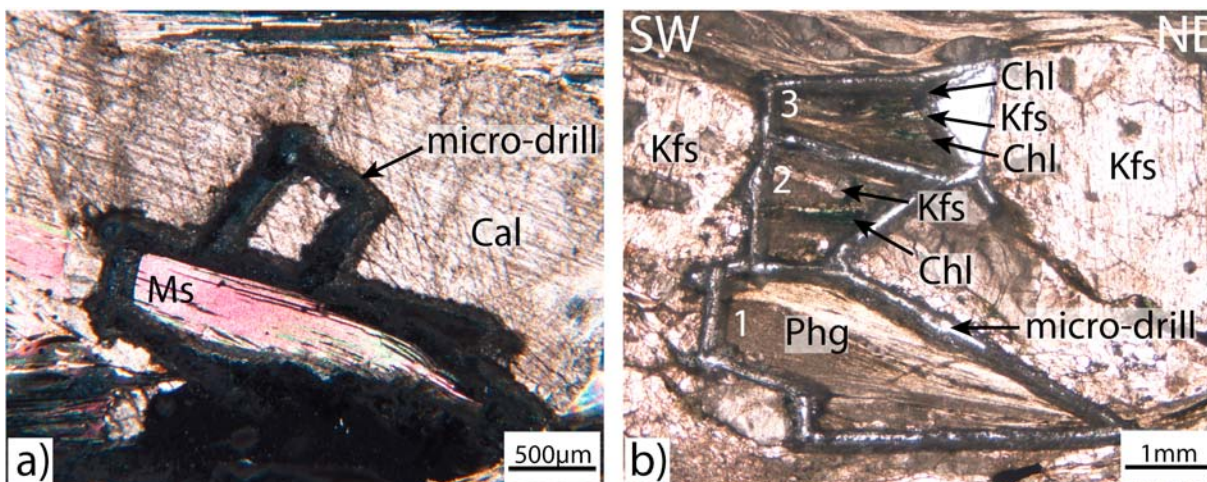


Figure 6. Rb/Sr microsampling methodology. (a) Microsampling of muscovite and calcite in textural contact from a vein in the neck of a foliation boudinage (MC492), region III. (b) Microsampling of synkinematic fibrous phengite in a stretched and fractured feldspar porphyroclast (MC472), region V.

4.1. Fission Track Analysis: Apatite and Zircon

[23] We analyzed 18 samples (16 from region IV and two from region II of the SFZ) from both the footwall and hanging wall along different sections across the fault zone. Details of separation methods and analysis techniques are given in Appendix A. Because of the extremely low uranium content of most of the apatite, not all apatite samples could be analyzed and track lengths could not be statistically measured. Most of the results from this study are therefore zircon fission track ages.

4.2. The $^{40}\text{Ar}/^{39}\text{Ar}$ Geochronology: White Mica and Biotite

[24] In the footwall, we collected samples at increasing distances from the detachment (SL), covering the transition from mylonitic rocks that were strongly affected by the Simplon shearing into the footwall protolith with little or no discernible overprint. A second set of samples was taken parallel to the SFZ, and reflects the increase in metamorphic grade from greenschist facies in the NW (Rhône Valley) to amphibolite facies in the SE (Ossola Valley). A similar sampling approach was also used in the hanging wall. In total, 21 samples were collected. This sampling strategy was chosen to consider whether it is deformation (and associated recrystallization) or temperature that exerts the most influence on the ages obtained. We separated deformed porphyroclasts of white mica and biotite from the Simplon mylonites (MC111, MC287, MC288, MC289, MC302 and MC499) and undeformed and annealed micas related to the $S_{1/2}$ fabric (MC283, MC286, MC290, MC292, MC366, MC506 and MC516). Samples were collected from both pre-Alpine basement units and their Mesozoic cover.

[25] In 5 additional samples, large flakes of white mica were separated from foliation boudinage veins (MC22, MC36, MC276, MC291, MC346). In samples MC420, MC422, and MC423, thin aggregates of synkinematic white

mica were separated. In MC420 (orthogneiss of the Aar massif) the thin synkinematic white mica could be differentiated from larger mica porphyroclasts and isolated under the binocular microscope. Methods of separation and analysis are summarized in Appendix B.

4.3. Rb/Sr Microsampling Geochronology

[26] A microsampling technique using rock thick sections was used [Müller *et al.*, 2000a, 2000b], allowing Rb/Sr dating of synkinematic mineral growth with direct microstructural control on the relationship to the Simplon deformation. Microsampling was carried out on samples from the necks of foliation boudinage and on fibers growing between segments of elongated and fractured porphyroclasts related to the Simplon stretching direction (Figure 2c).

[27] In three foliation boudinage samples from region III (Figure 3b), cogenetic synkinematic white mica and calcite could be separated in direct textural contact (Figure 6a samples MC492, MC494, MC497). Sample MC472 from region V consists of three adjacent microsamples of synkinematic fibrous white mica and/or quartz-feldspar-chlorite grown between segments of one stretched feldspar porphyroclast within a phyllonite of the Aar massif (Figure 6b). Microsampling and analysis methods are described in Appendix C.

4.4. Oxygen Isotope Thermometry

[28] Stable isotope-based thermometry is based on the temperature dependent isotope fractionation between two coexisting minerals, which for the case of oxygen is generally reported as

$$1000 \ln \alpha \approx \Delta_{1-2} = \delta^{18}\text{O}_1 - \delta^{18}\text{O}_2 = A(10^{18}/T^6) + B(10^{12}/T^4) + C(10^9/T^3) + D(10^6/T^2) + E(10^3/T) + F \quad (1)$$

Table 2. Representative Mica Compositions^a

Sample	SiO ₂	TiO ₂	Cr ₂ O ₃	Al ₂ O ₃	FeO	MnO	MgO	CaO	Na ₂ O	K ₂ O	Total
<i>White Mica</i>											
MC22	46.30	0.71	0.04	29.39	5.40	0.04	2.03	-	0.26	10.72	94.89
MC36	49.80	0.13	0.01	27.75	3.23	0.04	3.22	0.02	0.11	10.57	94.88
MC111	45.61	0.37	-	30.14	5.32	0.02	1.15	0.01	0.31	10.73	93.67
MC283											
S ₁	46.14	0.32	0.03	34.79	2.25	-	0.83	-	0.79	9.76	94.91
	50.30	0.18	0.02	28.39	3.60	-	2.44	-	0.26	9.78	94.97
S ₂	46.80	0.30	0.02	34.60	2.40	0.01	0.89	0.01	0.76	9.48	95.27
	50.09	0.18	0.04	28.62	3.61	0.03	2.44	-	0.31	9.82	95.13
MC286	47.28	0.82	0.01	35.65	1.71	-	0.79	-	0.52	10.16	96.94
	48.16	1.21	0.03	32.55	1.95	-	1.52	-	0.40	10.19	96.01
	51.80	0.54	-	28.25	2.32	0.02	2.84	-	0.24	10.30	96.30
MC287	47.62	1.00	-	29.62	5.23	0.04	1.62	-	0.23	10.76	96.12
MC288	47.43	0.85	0.06	34.31	0.88	-	1.63	0.14	0.40	10.49	96.19
MC289	47.27	1.67	-	29.77	5.31	0.05	1.76	-	0.24	9.82	95.89
MC290	47.71	0.45	-	33.50	3.75	0.02	0.46	-	0.41	10.52	96.82
	48.50	0.36	0.01	32.54	4.18	0.09	0.59	-	0.22	10.46	96.95
	49.48	0.30	-	31.74	4.62	0.07	0.74	0.05	0.24	10.32	97.57
MC292	46.64	0.65	0.11	35.16	1.06	-	0.72	0.01	0.98	9.19	94.51
MC302	46.90	0.33	0.04	34.05	2.19	0.01	0.86	-	1.10	9.34	94.82
	46.92	0.21	-	35.81	1.41	0.01	0.51	0.01	2.22	7.64	94.73
	48.32	0.27	0.02	29.92	2.18	0.01	1.76	-	0.87	9.26	92.61
MC366	46.70	0.47	0.01	35.90	2.03	0.02	0.66	0.01	0.99	9.35	96.14
MC420	48.57	0.19	-	28.40	2.84	0.03	2.67	0.03	0.20	10.75	93.68
	49.73	0.11	-	26.80	2.59	0.04	3.09	0.03	0.10	10.78	93.27
	50.90	0.03	-	24.99	2.55	0.05	3.75	-	0.07	10.88	93.22
MC422	48.46	0.15	0.01	26.38	3.44	0.04	3.42	0.01	0.08	11.00	92.99
MC423	47.37	0.41	0.05	33.18	1.26	-	1.44	0.01	0.24	10.62	94.57
MC492	45.91	0.71	0.01	29.19	5.10	0.01	1.99	-	0.30	10.92	94.13
MC494	45.24	0.80	0.02	28.73	4.91	-	2.11	-	0.28	10.87	92.96
MC506	46.44	0.71	0.04	34.29	1.19	-	0.82	-	1.19	9.37	94.05
MC516	46.66	0.16	0.02	34.49	0.23	-	1.36	-	1.21	9.51	93.64
<i>Biotite</i>											
MC420	37.95	1.96	0.12	15.27	16.83	0.24	12.57	0.01	0.04	9.73	94.72
MC499	37.43	2.36	0.03	17.06	16.41	0.31	12.39	0.01	0.07	9.91	95.97

^aS₁ and S₂ are foliations related to the D1 and D2 deformation phases [Milnes *et al.*, 1981].

where T is the absolute temperature, and A, B, C, D and F are calibrated coefficients. In this study we calculate the fractionation of $\delta^{18}\text{O}$ on coeval pairs of quartz and white mica in three calcite-quartz-white mica rich veins (samples MC494, MC497 and MC498) using the following coefficients: A = -0.0086, B = 0.042, C = 0.000, D = 1.350, E = 0.00 and F = 0.00 [Chacko *et al.*, 1996]. Further details of the method are given in Appendix D.

4.5. Petrological and Chemical Description of Samples Used for ⁴⁰Ar/³⁹Ar, Rb/Sr and Oxygen Isotope Analysis

[29] Table 1 gives a concise structural description of the samples. All micas were first analyzed by electron microprobe and representative compositions are given in Table 2.

[30] Samples typical of the amphibolite facies Simplon mylonites in the footwall (MC302, MC287, MC288, MC289, MC111 and MC499) have deformed porphyroclasts of mica defining the foliation plane and show shear bands with a top-to-SW sense of shear (Figure 7a). White mica often forms mica fish (Figure 7b). Mica flakes can be quite large, with a diameter on average of ~400 μm to 1 mm. The undeformed sample MC366 (coming further east from the core of the Toce Dome) and samples MC286, MC290, MC292, MC506 and MC516 (from the hanging

wall) do not show any overprint from the Simplon shear zone. Micas, with a diameter of ~200 μm to 1 mm (Figures 7c and 7d), define the S_{1/2} foliation plane and are interlayered with recrystallized quartz and plagioclase. Mica grain boundaries are annealed, and grains show little internal deformation. Sample MC283 from the greenschist facies region of the hanging wall shows two schistosity marked by aligned white micas (Figure 7e). The S₁ schistosity is crenulated, with folded and kinked white micas, whereas the second schistosity S₂ defines the crenulation cleavage with new undeformed white micas growing in the axial plane. Both generations have a similar diameter of ~400–500 μm (Figure 7e). It was not possible to separate these two generations of micas.

[31] For all these samples, white micas have muscovite compositions [Rieder *et al.*, 1998] (Table 2). In the amphibolite facies region, single muscovite from both footwall and hanging wall are not zoned in major elements and the Tschermak substitution [Guidotti, 1973] in each sample is quite small (Figure 8a), with a relatively homogeneous composition (MC366, MC287, MC288, MC289, MC111, MC292, MC506 and MC516). In contrast, closer to the greenschist facies region, the Tschermak substitution is more important (MC302, MC290, Figure 8b), and muscovites are slightly zoned in major elements. In the greenschist

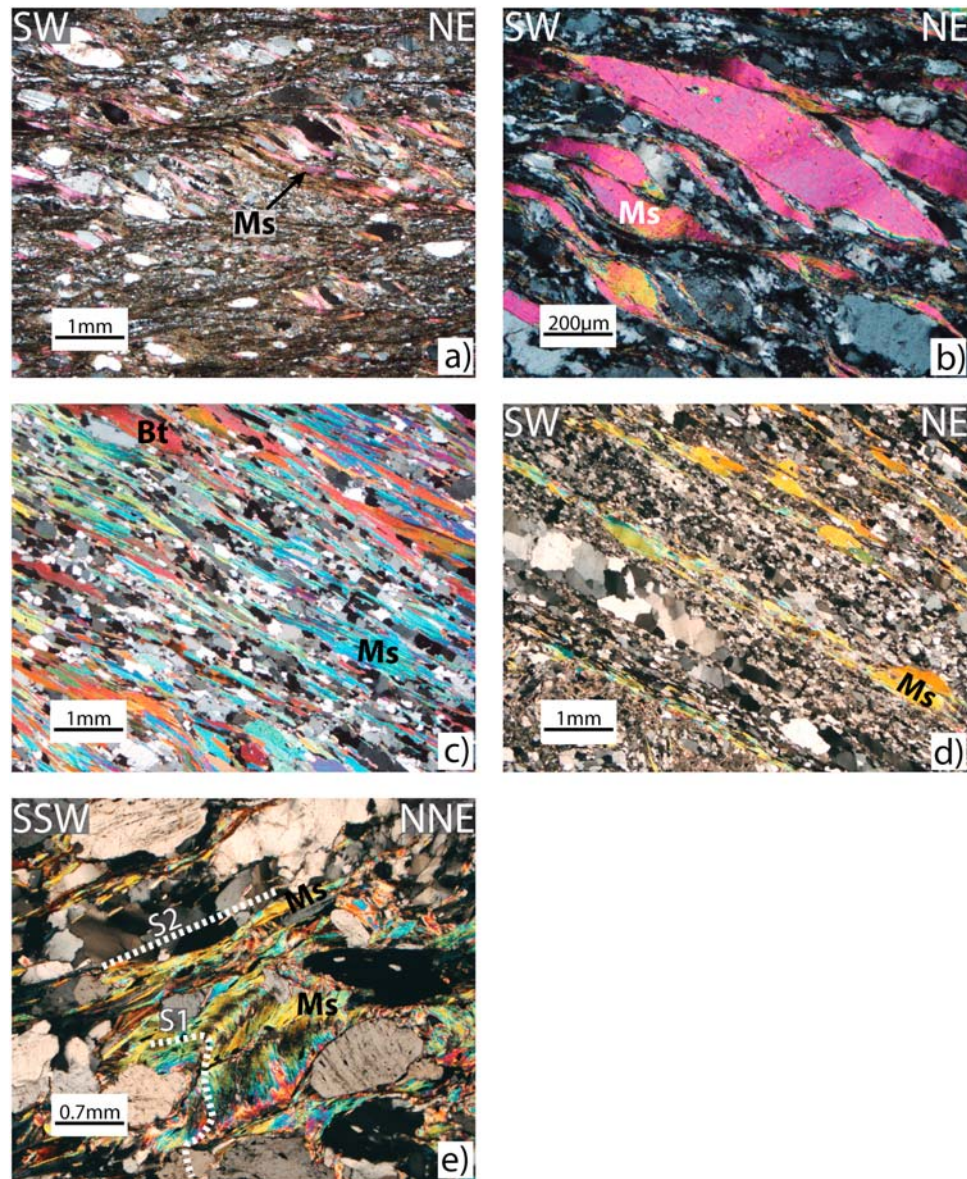


Figure 7. Sample description. (a) Simplon mylonites from the amphibolite facies region (region II) with deformed porphyroclasts of white mica affected by shear bands with a clear sense of shear top-to-SW (MC287). (b) Mica fish within the Simplon mylonites from the region II; note the undulose extinction within the mica (MC287). (c) Undeformed annealed micas from a sample not affected by the Simplon shearing (MC366), within the Toce Dome. (d) Undeformed annealed micas from a sample not affected by the Simplon shearing (MC286), from the hanging wall. (e) Two generations of white mica (MC283), from the hanging wall.

facies region of the hanging wall, muscovites show a clear zonation in major elements (MC283 and MC286), and the Tschermak substitution is strongly developed (Figure 8b). In the greenschist facies, muscovites are not homogeneous within one sample or even within one single grain (Figure 8b).

[32] Samples from quartz-calcite-white mica veins in region III (MC22, MC276, MC291, MC346, MC492, MC494, MC497 and MC498) all come from amphibolite facies mylonites (Sm) developed in Monte Leone orthogneiss of the footwall (Figure 5). MC22, MC276, MC346,

MC492 and MC494 are undeformed veins filling the necks of foliation boudinage. In thin section, the quartz and white mica show only slight undulose extinction (Figure 9a) and are otherwise undeformed. The vein MC291 is deformed and rotated in a dextral sense toward the foliation as a flanking structure. MC497 and MC498 are veins with Riedel fault orientations coming from boulders of the Monte Leone unit, found in the Isorno River (region III). Their relation to the foliation and stretching lineation is identical to that in the immediately adjacent outcrops. In all these veins, calcite

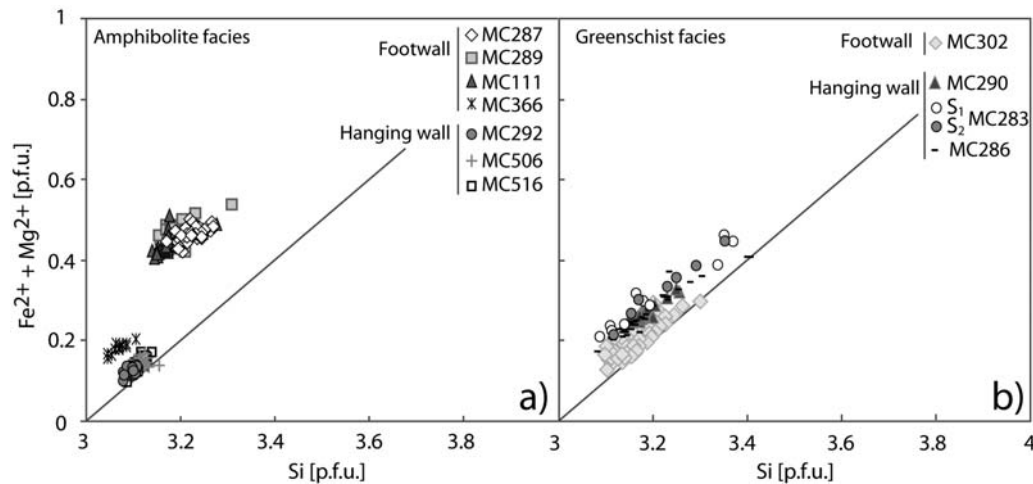


Figure 8. Tschermak substitution for the analyzed white micas. (a) Muscovites from the amphibolite facies region. (b) Muscovites from the greenschist facies region. Normalization to 11 oxygen per formula unit.

(≥ 1 mm), quartz and white mica (> 1 mm) are in textural contact (Figure 9a). Similar muscovite compositions [Rieder *et al.*, 1998] were obtained for the three undeformed veins (MC22, MC492 and MC494, Table 2) and there is no variation or zonation in composition within single grains (Figure 9b).

[33] Samples MC36, MC420, MC422, MC423 and MC472 from the Rhone Valley (region V) are foliated phyllonites, developed from orthogneisses of the Aar Massif and its cover. White mica forms very thin flakes ~ 30 – $140 \mu\text{m}$ in length and 2 – $40 \mu\text{m}$ in width that define the foliation plane (Figure 10a), and develop from the destabilization of feldspar under fluid-present conditions [Rossi *et al.*, 2005; Rolland *et al.*, 2008] (Figure 10b). These synkinematic white micas are clearly affected by

dextral shearing, as indicated by overprinting shear bands (Figure 4b) and grow as fibers between broken porphyroclasts of feldspar (Figure 10b). Large porphyroclasts of biotite, with a diameter of ~ 400 – $700 \mu\text{m}$, can also be found in some samples (MC420) (Figure 10c). Biotite is deformed, folded and kinked, and shows undulose extinction. For three analyzed phyllonites (MC36, MC420, and MC422), white micas have similar phengitic compositions [Rieder *et al.*, 1998], with the average given in Table 2. Such phengitic compositions developed under low pressure conditions and probably reflect fluid-rock interaction similar to that described in shear zones from the Mt Blanc massif by Rossi *et al.* [2005] and Rolland *et al.* [2008] and from the Aar Massif in the Grimsel Pass area by Rolland *et al.* [2009]. Sample MC423 from the cover of the Aar Massif has a different

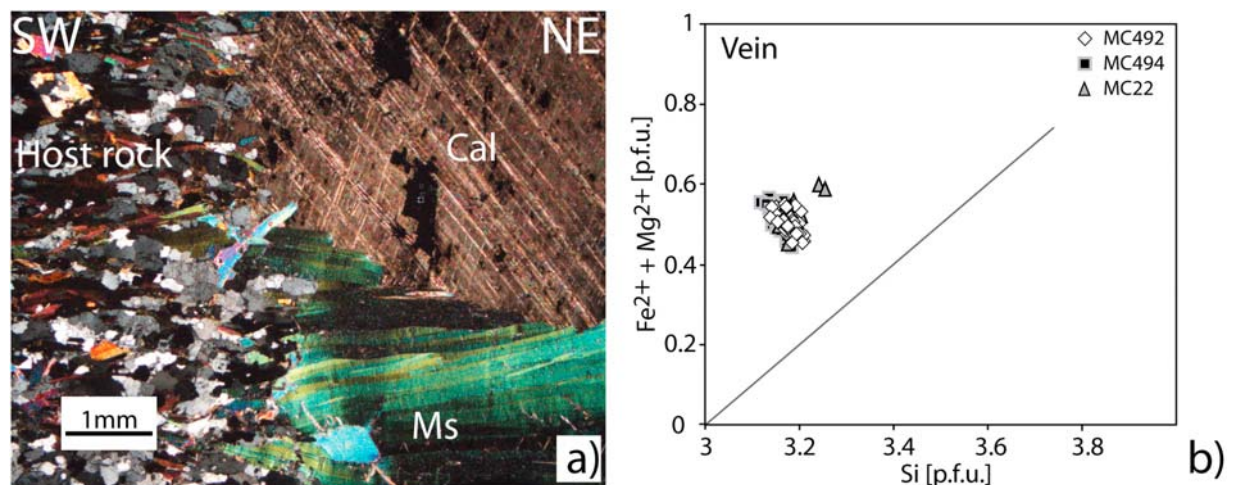


Figure 9. Veins from region III (a) calcite (Cal) and muscovite (Ms) from a vein filling the neck of foliation boudinage (MC492), region III. (b) Tschermak substitution for the analyzed muscovites from veins in the neck of foliation boudinage. Normalization to 11 oxygens per formula unit.

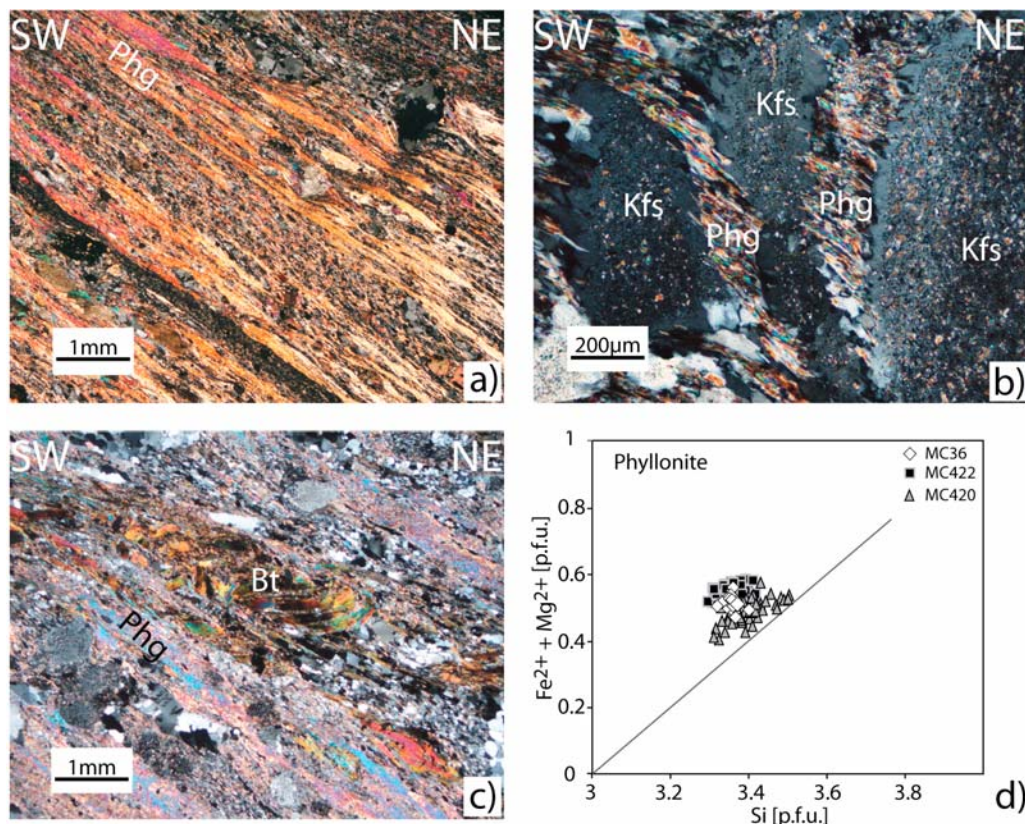


Figure 10. Phyllonites from region V. (a) Phyllonite development from orthogneiss of the Aar massif, with a matrix composed of very thin phengite (Phg) (MC36). (b) Fibers of phengite between broken feldspar (K-feldspar, Kfs) porphyroclasts (MC36). (c) Deformed porphyroclasts of biotite (Bt) within the phyllonite (MC420). (d) Tschermak substitution for the analyzed phengites from phyllonites of the Aar massif. Normalization to 11 oxygens per formula unit.

composition (Table 2), reflecting the different bulk rock composition. For each phyllonite, single grains show no zonation in composition, and we observe only small variations in Tschermak substitution (MC420, Figure 10d).

5. Results

5.1. Fission Track Analysis

[34] Twenty-three new fission tracks ages are presented in Table 3 and Figure 5 with apatite ages ranging from 3 to 6 Ma and zircon ages from 10 to 20 Ma. Overall, zircon central ages are younger in the footwall (9.7 to 14 Ma) than in the hanging wall (13.7 to 19.9 Ma). In the SE (region II), samples MC500 and MC501 show a clear jump of 5.5 Ma in zircon ages across the SL over a distance of 570 m, with ages of 12.9 Ma in the footwall and 18.4 Ma in the hanging wall (Figure 5). In the NW (region IV), a similar jump in zircon ages of 5.8 Ma over 260 m is recorded, with ages of 12.4 Ma (MC475) in the footwall and 18.2 Ma (MC476) and 17.2 Ma (MC477) in the hanging wall (with these last two samples being indistinguishable within 1σ error) (Figure 5). However, except for these samples, in region IV a single clear jump in zircon ages can no longer be established. Instead, ages increase gradually toward the hanging wall.

5.2. The $^{40}\text{Ar}/^{39}\text{Ar}$ Geochronology

[35] The $^{40}\text{Ar}/^{39}\text{Ar}$ ages are presented in Table 4 and Figures 5 and 11. The detailed analytical data set is available in the auxiliary material.¹ White mica $^{40}\text{Ar}/^{39}\text{Ar}$ ages range from 11 to 22.5 Ma, and one biotite yielded an age of 15.2 Ma (Table 4 and Figures 5 and 11). Two samples from basement units have older apparent ages reflecting some pre-Alpine inheritance: biotite porphyroclasts (MC420) in the Aar massif with a total release age of 67 Ma, and muscovite MC286 from the hanging wall with 79 Ma (Figure 5). These two greenschist facies samples, as well as MC283 (22.5 Ma in the hanging wall), also show very disturbed spectra (Figures 11g, 11h, and 11i). Samples from the amphibolite facies of both the footwall and the hanging wall generally yield plateau ages (Table 3 and Figures 11a, 11b, 11c, 11d, and 11f), and white mica $^{40}\text{Ar}/^{39}\text{Ar}$ ages from the basement unit (MC287, MC289, MC111, MC366) and its cover (MC288) yield a similar range of ages between 20 and 14 Ma. Except for samples MC286 and MC420 with some pre-Alpine inheritance, $^{40}\text{Ar}/^{39}\text{Ar}$ ages are generally

¹Auxiliary materials are available at <ftp://ftp.agu.org/apend/tc/2009TC002582>.

Table 3. Fission Track Ages^a

Sample	Mineral	Number of Crystals	Track Density ($\times 10^5 \text{ cm}^{-2}$)			Uranium (ppm)	P(χ^2) (Var %)	FT Age $\pm 2\sigma$ (Ma)
			ρ_d (Counted)	ρ_i (Counted)	ρ_s (Counted)			
MCS3	Apatite	40	14.45 (7924)	11.14 (1621)	0.13 (19)	8	2 (0.4)	3.2 \pm 1.6
	Zircon	30	5.12 (1655)	40.82 (1826)	13.79 (617)	279	0 (0.3)	11.4 \pm 1.8
MCS8	Zircon	20	4.69 (1655)	26.92 (884)	18.18 (597)	203	0 (0.3)	19.9 \pm 3.2
MCS12	Zircon	26	4.46 (1655)	24.14 (925)	11.72 (449)	180	32 (0.1)	14.0 \pm 1.8
MC33	Apatite	35	11.55 (7924)	10.15 (1417)	0.22 (31)	10	8 (0.4)	4.4 \pm 1.8
	Zircon	26	3.91 (1655)	28.59 (1232)	18.75 (808)	240	4 (0.2)	16.5 \pm 2.0
MC269	Zircon	20	4.20 (2833)	29.67 (1138)	12.54 (481)	229	6 (0.2)	11.6 \pm 1.6
MC282	Zircon	20	4.03 (2833)	21.57 (625)	11.87 (344)	172	0 (0.3)	15.0 \pm 3.0
MC335	Zircon	20	3.83 (2419)	25.50 (677)	11.30 (300)	265	4 (0.3)	10.9 \pm 2.2
MC283	Zircon	21	4.97 (3150)	24.20 (492)	13.08 (266)	162	31 (0.2)	17.4 \pm 3.0
MC475	Apatite	20	12 (8084)	9.54 (780)	0.25 (20)	9	74 (0)	5.3 \pm 2.4
	Zircon	21	4.58 (3150)	28.08 (595)	11.47 (243)	204	8(0.2)	12.4 \pm 2.4
MC476	Zircon	28	4.01 (2419)	18.88 (626)	13.24 (439)	155	4 (0.2)	18.2 \pm 3.0
MC477	Zircon	22	3.92 (2419)	20.40 (682)	13.82 (462)	170	48 (0)	17.2 \pm 2.2
MC480	Zircon	20	4.59 (2777)	38.57 (896)	18.34 (426)	267	10 (0.2)	14.1 \pm 2.2
MC481	Zircon	24	3.73 (2419)	17.70 (758)	10.02 (429)	152	76 (0)	13.7 \pm 1.8
MC482	Zircon	22	4.31 (2777)	36.22 (759)	12.79 (268)	283	1 (0.3)	9.7 \pm 2.0
MC500	Apatite	20	14.38 (8084)	15.46 (1740)	0.19 (21)	12	57 (0)	3.0 \pm 1.4
	Zircon	20	5.21 (3150)	109.61 (2130)	41.73 (811)	665	23 (0.1)	12.9 \pm 1.2
MC501	Apatite	21	14.04 (8084)	20.23 (2078)	0.47 (48)	16	58 (0)	5.5 \pm 1.6
	Zircon	20	5.47 (3150)	79.37 (1679)	40.99 (867)	465	3 (0.1)	18.4 \pm 2.0
MC519	Zircon	20	4.36 (2777)	21.80 (617)	12.72 (360)	159	84 (0)	16.5 \pm 2.2
MC520	Zircon	21	4.49 (2777)	20.32 (538)	13.26 (351)	160	7 (0.2)	19.0 \pm 3.4

^aThe parameters ρ_s and ρ_i represent sample spontaneous and induced track densities; P(χ^2) is the probability of χ^2 for ν degrees of freedom where ν is number of crystals minus 1. All ages are central ages [Galbraith, 1981] and are reported with a 2σ error. $\lambda D = 1.55125 \times 10^{-10}$. Ages were calculated using the recommended ζ calibration approach [Hurford and Green, 1983]. A geometry factor of 0.5 was used. $\zeta = 341 \pm 6$ for CN5/apatite and 130 ± 0.6 for CN1/zircon. Uranium concentration is a broad approximation with an error minimum $>20\%$.

younger in the footwall than in the hanging wall. In the footwall parallel to the fault, ages for white mica tend to decrease from SE (20–14 Ma) to NW (14–11 Ma) toward the greenschist facies region. In the amphibolite facies region, muscovite ages also tend to decrease from 20 to 17 Ma to 15–14 Ma with increasing distance from the SL (i.e., with decreasing shearing overprint and increasing depth of exhumation).

[36] In the SE (region III), ages for three muscovites from the necks of foliation boudinage give 14 Ma (MC22, MC276 and MC346) (Figure 11d). This age is identical within error to that obtained on white mica from similar veins in the same area by Purdy and Stalder [1973] using traditional K/Ar methods. Muscovite from the vein showing flanking structure development (MC291) gives a slightly older age of 15.9 Ma (Figure 11d). This age is similar to the age of 16 Ma obtained for the muscovite from the host rock (MC111). Biotite (MC499) from the host rock gives 15 Ma (Figure 11a), which is slightly younger than muscovite (MC111).

[37] In the Rhone Valley (region V), 4 aggregates of very thin phengites from different phyllonites all give very similar narrow staircase spectra that increase from 10 Ma to 14 Ma (Figure 11j). Samples MC422 and MC36 yielded older ages for the first and final steps of the spectra (Figure 11j).

5.3. Rb/Sr Geochronology

[38] In the SE (region III), Rb/Sr ages from two veins within the neck of foliation boudinage (MC492 and MC494) and from a Riedel structure (MC497) all give similar ages of

circa 14.5 Ma, almost identical to $^{40}\text{Ar}/^{39}\text{Ar}$ ages on similar veins (Table 5 and Figures 5, 11d, and 12). Ages represent two-point Rb/Sr ages using microdrilled muscovite-calcite pairs (Figures 12a and 12b). These results are confirmed by the isochron age (MC 492) obtained by using several measurements on muscovite-calcite pairs from the same sample (Figure 12c).

[39] In the NW (region V), three microsamples of synkinematic fibrous phengite from a stretched feldspar porphyroclast are not tightly colinear, resulting in an age with a very large 2σ error (14.6 ± 9.5 Ma; Figure 12d). It is possible that isotopic equilibrium was not achieved between all three microsamples, considering also the presence of small inclusions within microsamples 2 and 3 (Figure 6b and Table 5). The two-point Rb/Sr age between microsamples 1 (pure phengite) and 2, which are in textural contact (Figure 12d), would be 14.5 ± 0.12 Ma, comparable with $^{40}\text{Ar}/^{39}\text{Ar}$ ages on the same structures (Figure 11j). Including microsample 3 (which is not in textural contact) does not significantly change the best fit age, but markedly increases the 2σ error.

5.4. Oxygen Stable Isotope Analysis

[40] Oxygen isotope data are presented in Table 6 with values representing averages of at least two replicate measurements from the same mineral separate. Using isotopic fractionation for cogenetic quartz-muscovite pairs from three different veins at the same general location, we calculate equilibrium temperatures of $394 \pm 20^\circ\text{C}$, $386 \pm 30^\circ\text{C}$ and $406 \pm 12^\circ\text{C}$ in the veins MC494, MC497, and MC498,

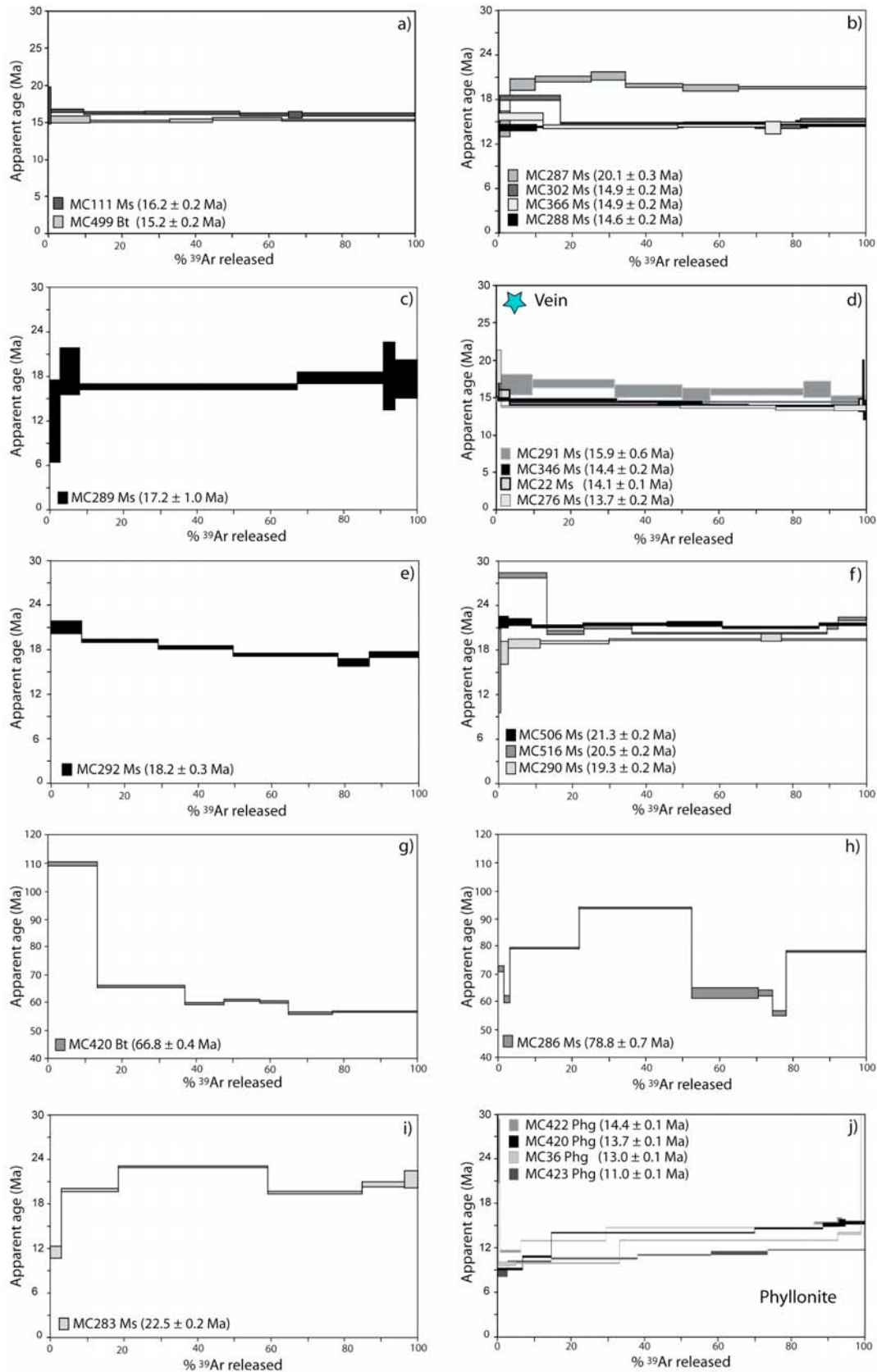


Figure 11. The $^{40}\text{Ar}/^{39}\text{Ar}$ age spectra for each sample. Bt, biotite; Ms., muscovite; Phg, phengite. The detailed analytical data set is available in the auxiliary material.

Table 4. The $^{40}\text{Ar}/^{39}\text{Ar}$ Ages^a

Sample	Mineral	PS (TS)	$^{39}\text{Ar}_k$ (%)	$^{40}\text{Ar}/^{39}\text{Ar}$ Age $\pm 2\sigma$ (Ma)	Description
MC22	Muscovite	3–6 (8)	95.6	14.1 \pm 0.1	Plateau age
MC36	Phengite			13.0 \pm 0.1	Total release age
MC111	Muscovite	2–7 (7)	99.3	16.2 \pm 0.2	Plateau age
MC276	Muscovite	2–5 (5)	98.8	13.7 \pm 0.2	Plateau age
MC283	Muscovite			22.5 \pm 0.2	Total release age
MC286	Muscovite			78.8 \pm 0.7	Total release age
MC287	Muscovite	2–7 (7)	96.9	20.1 \pm 0.3	Plateau age
MC288	Muscovite	2–5 (5)	89.6	14.6 \pm 0.2	Plateau age
MC289	Muscovite	2–6 (6)	97.2	17.2 \pm 1.0	Plateau age
MC290	Muscovite	3–7 (7)	97.4	19.3 \pm 0.2	Plateau age
MC291	Muscovite	2–6 (7)	81.2	15.9 \pm 0.6	Plateau age
MC292	Muscovite			18.2 \pm 0.3	Total release age
MC302	Muscovite	4–6 (6)	83.1	14.9 \pm 0.2	Plateau age
MC346	Muscovite	1–3 (3)	100	14.4 \pm 0.2	Plateau age
MC366	Muscovite	2–5 (5)	87.8	14.9 \pm 0.2	Plateau age
MC420	Phengite			13.7 \pm 0.1	Total release age
	Biotite			66.8 \pm 0.4	Total release age
MC422	Phengite			14.4 \pm 0.1	Total release age
MC423	Phengite			11.0 \pm 0.1	Total release age
MC499	Biotite	2–6 (6)	99.8	15.2 \pm 0.2	Plateau age
MC506	Muscovite	1–7 (7)	100	21.3 \pm 0.2	Plateau age
MC516	Muscovite	2–4 (6)	76.2	20.5 \pm 0.2	Plateau age

^aPS, number of steps constituting the plateau; TS, total number of steps in the spectra; $^{39}\text{Ar}_k$, the percentage of accumulated ^{39}Ar released in the plateau. The detailed analytical data set is available in the auxiliary material.

respectively. As is clear, the results from the three veins are the same within one standard deviation for the repeat analyses, with a mean value around 395°C.

6. Discussion

6.1. Fission Track Ages and the Brittle History of the Simplon Fault Zone: The “Simplon Line”

[41] In the NW (region IV), zircon fission track ages gradually increase toward the hanging wall (Figure 5). This implies a continuation of the Simplon Line (SL) not as one single discrete fracture but as a wider zone of deformation, with the brittle detachment divided into several branches. The overall relative displacement between footwall and hanging wall is similar to that in region I [Steck and Hunziker, 1994], but is not localized on one single detachment. Field observations support this interpretation, with a wide zone of brittle deformation observed in this region (Figure 4). We interpret region IV to reflect a relatively high structural level of the low-angle detachment system. Zircon fission track ages obtained from this section imply that the fault was still active at about 11 Ma. However, our data suggest that a jump in apatite fission track ages is not developed in this region, although it must be considered that apatite with low uranium content has a very large error and could hide any possible jump. The new zircon fission track ages therefore confirm that there is a continuation of the SL in the Rhone Valley (region V), where a clear jump in apatite fission track ages has also been described [Soom, 1990; Seward and Mancktelow, 1994].

[42] The single clear jump in zircon and apatite fission track ages observed in region II confirms that the SL was still active at circa 12 Ma and probably until around 3 Ma. There is no discernible jump in fission track ages [Keller et al., 2005b] across the projected continuation of the SL

toward the SE, in regions II and III (Figure 2a). We interpret this to reflect a change to dextral strike slip kinematics, without any significant differential exhumation between footwall and hanging wall, as suggested by the near horizontal stretching lineations (Figure 2c). Keller et al. [2006] argue that the fault may no longer exist in this region and that displacement has instead been accommodated by back folding in the Camughera-Moncucco unit. In our opinion this hypothesis is not tenable. First, it would imply decreasing displacement along the SL toward region II. However, a similar discontinuity in zircon fission track ages is observed along the NW-SE striking segment of the SL (with a strictly normal component) from circa 18 to 12 Ma (Figure 5). The proposed geometry would also imply a rotation of the hanging wall, and there are no field observations to support such a rotation, with measured stretching lineations maintaining the same orientation (see Figure 2c).

6.2. The $^{40}\text{Ar}/^{39}\text{Ar}$ and Rb/Sr Data: Cooling or Neo-(Re-)crystallization Ages?

[43] The significance of mica $^{40}\text{Ar}/^{39}\text{Ar}$ and Rb/Sr ages in mylonites is strongly debated and ages are generally explained as due to either (1) thermally activated diffusion of daughter and/or parent isotopes, leading to the concept of a specific closure temperature for an isotopic system in a particular mineral [Jäger, 1965; Jäger et al., 1967; Dodson, 1973] or (2) neocrystallization and recrystallization related to deformation and/or fluid-rock interaction, associated with grain size reduction and/or interlayered mica growth [e.g., Dunlap, 1997; Villa, 1998; Mulch and Cosca, 2004; Mulch et al., 2005].

[44] In an attempt to resolve these potentially quite different interpretations of age results in the Simplon region, both deformed single mica porphyroclasts from the vicinity

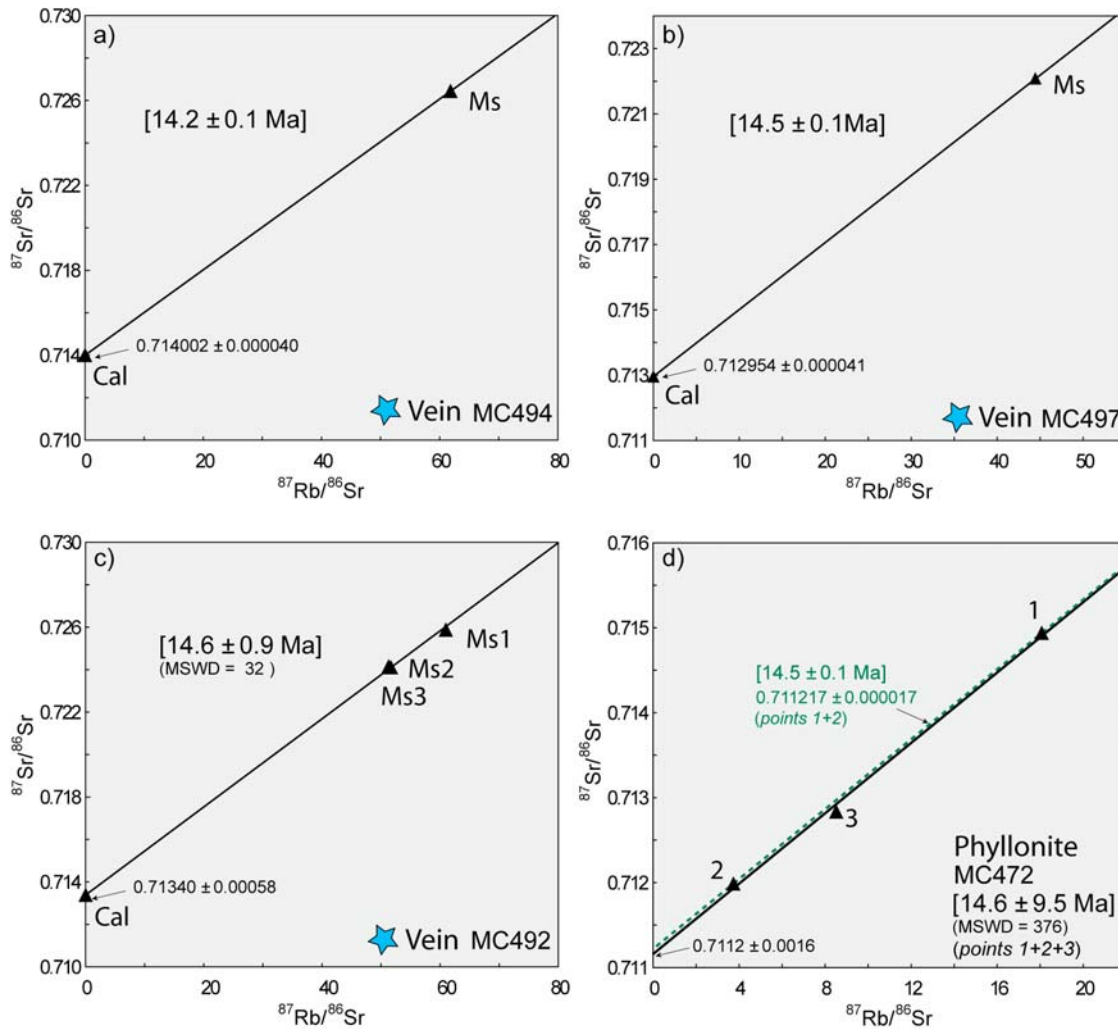


Figure 12. Two-point and isochron Rb/Sr microsampling ages. Ms, muscovite; Cal, calcite.

of the fault, which are in part internally recrystallized (Figures 7a and 7b), and annealed micas from outside the shear zone (Figures 7c and 7d) were analyzed by $^{40}\text{Ar}/^{39}\text{Ar}$ geochronology. Within the amphibolite facies, both mica types yield a similar range of ages: (1) deformed porphy-

roclasts related to the SFZ range from 20.1 to 14.6 Ma (MC111, MC302, MC287, MC288, MC289, MC499; Figure 5) and (2) undeformed and annealed micas range from 21.3 to 14.9 Ma (MC290, MC292, MC366, MC506; Figure 5). All these samples from the amphibolite facies

Table 5. Rb/Sr Microsampling Isotopic Data^a

Sample	Mineral Pairs	Sample Weight (μg)	Rb (ppm)	Sr (ppm)	$^{87}\text{Rb}/^{86}\text{Sr}$	$^{87}\text{Sr}/^{86}\text{Sr} \pm 2\sigma$	$(^{87}\text{Sr}/^{86}\text{Sr})_i \pm 2\sigma$	Age $\pm 2\sigma$ (Ma)
MC494	Ms	883	174.88	8.20	61.843	0.726444 ± 0.000048	0.714002 ± 0.00004	14.17 ± 0.07
	Cal	67	0.53	277.80	0.00552	0.714003 ± 0.000041		
MC497	Ms	720	247.74	16.15	44.435	0.722078 ± 0.000049	0.712954 ± 0.00004	14.46 ± 0.10
	Cal	79	0.25	458.40	0.00160	0.712954 ± 0.000042		
MC492	Ms 1	575	247.64	11.78	60.930	0.725888 ± 0.000041	0.713400 ± 0.00060	14.58 ± 0.86
	Ms 2	427	249.22	13.98	51.670	0.724102 ± 0.000079		
	Ms 3	397	239.07	13.51	51.289	0.724160 ± 0.000053		
	Cal	49	1.00	336.40	0.00861	0.713377 ± 0.000055		
MC472	1-Phg	1638	591.28	94.74	18.069	0.714937 ± 0.000010	0.711200 ± 0.00165	14.6 ± 9.5
	2-Phg+Chl+Kfs	560	275.14	213.50	3.731	0.711985 ± 0.000014		
	3-Phg+Chl+Kfs	608	397.15	135.10	8.512	0.712833 ± 0.000010		

^aMs, muscovite; Cal, calcite; Phg, phengite.

Table 6. Oxygen Stable Isotope Data^a

Sample	$\delta^{18}\text{O}_{\text{qtz}}$ (‰)	$\delta^{18}\text{O}_{\text{ms}}$ (‰)	$\Delta\text{qtz-ms}$	Temperature (°C)
MC494	12.25	9.09	3.15	394 ± 20
MC497	11.23	8.01	3.22	386 ± 30
MC498	11.08	8.05	3.04	406 ± 12

^aValues represent an average of selected replicate measurements from the same mineral separate. Uncertainties on the temperature are calculated from the standard deviation of replicates. qtz: quartz; ms: muscovite.

region have reached a minimum temperature of ~500°C at circa 30 Ma [Frank, 1983; Vance and O’Nions, 1992; Todd and Engi, 1997] prior to SFZ deformation. Recrystallization should produce younger ⁴⁰Ar/³⁹Ar ages within the Simplon shear zone. As similar ages are found in both deformed (and in part recrystallized) and undeformed micas, we consider that cooling rather than recrystallization was responsible for the observed ⁴⁰Ar/³⁹Ar ages in the amphibolite facies. The regional Lepontine metamorphism has caused reequilibration of the major element mica composition, annealed previous structures in old micas (Figures 7c and 7d) and promoted the growth of new mica grains. Subsequently, these micas were deformed in the SFZ following a retrograde path, starting under rather high temperature conditions of amphibolite facies (>500°C, with peak temperatures to the SE of 580–620°C [Frank, 1983; Vance and O’Nions, 1992; Todd and Engi, 1997]).

[45] Ar diffusion in mica is still a controversial topic and closure temperatures for micas are not well determined [e.g., Dodson, 1973; Hames and Bowring, 1994; Villa, 1998; Harrison et al., 2009]. By solving the solid state diffusion equation of Dodson [1973] using the diffusion parameters of Hames and Bowring [1994] ($E\alpha = 52$ kcal/mol; $D_0 = 0.04$ cm²/s), an estimated cooling rate of 30°C/Ma [Campani, 2009], a grain size of 500 μm, and a cylindrical geometry, we obtain a closure temperature of ~440°C for muscovite. This estimated closure temperature is slightly less than the minimum temperatures interpreted for the amphibolite facies samples (>500°C) and significantly less than peak metamorphic temperatures in the footwall at the start of exhumation (580–620°C).

[46] Muscovite from veins in the Isorno Valley (region III) give ⁴⁰Ar/³⁹Ar ages younger (14 Ma) than both muscovite and biotite from the host rocks. Similar ages of circa 14.5 Ma were also obtained on such veins by Rb/Sr microsampling. This suggests that the 14 Ma ⁴⁰Ar/³⁹Ar ages from the veins reflect crystallization of newly grown white mica in veins that developed in the necks of foliation boudins. This interpretation is consistent with the equilibration temperature of ~395°C obtained from stable oxygen isotope analyses on quartz-muscovite pairs from these veins. This temperature is significantly below the estimated closure temperature of ~480°C for the ⁴⁰Ar/³⁹Ar system in white micas from this region. If white mica grows under such conditions, the age should retain the time of crystallization [e.g., Dunlap, 1997]. The composition of muscovite within each vein is homogeneous and thus the age of one single grain should be representative of the sample. The older, more strongly rotated and deformed vein (flanking structure) MC291, has a

similar ⁴⁰Ar/³⁹Ar age to the muscovite from the host rocks (16 Ma), and this age is probably also a cooling age. These veins developed progressively during ongoing shearing and cooling through time, so earlier veins should have formed at higher temperature than the later veins.

[47] In the greenschist facies region, in the Rhone Valley and in the hanging wall (Figure 1a), peak metamorphic temperatures never exceeded 400 to 420°C [Frank, 1983]. Pre-Alpine porphyroclasts of biotite (MC420) and white mica (MC286), from the Aar massif and the hanging wall respectively, show very disturbed spectra, with ⁴⁰Ar/³⁹Ar ages varying between pre-Alpine and Alpine. This can either be interpreted as due to (1) the presence of a mixture of pre-Alpine white mica intimately intermingled with some fine neocrystallized Alpine white mica or (2) a partial loss of ⁴⁰Ar during Alpine deformation, at temperatures that were not high enough (or deformation that was not pervasive enough) to fully degas argon from the grains. Muscovite MC283 from the hanging wall has an apparent age of 22.5 Ma, but with a release spectrum for which no properly defined plateau age could be calculated. The result probably reflects a mixed age from the two generations of white mica (S_1 and S_2) actually observed in the sample, but could also be due to partial loss of ⁴⁰Ar during the second deformation D2 or to thermal advection from the exhuming footwall of the SFZ, as proposed by Markley et al. [1998].

[48] The different age patterns obtained in the amphibolite facies (with young Alpine ages) compared to the greenschist facies (with partially reset pre-Alpine ages) (Figure 5) is in good agreement with the results of Frank and Stettler [1979], who have suggested that the release patterns of their ⁴⁰Ar/³⁹Ar samples were controlled by the metamorphic grade. New mica that grew under greenschist facies conditions should preserve the crystallization age [Dunlap, 1997]. In fact, in the Rhone Valley (region V), very thin phengites in phyllonite developed from orthogneiss of the Aar Massif and its cover do record Alpine ⁴⁰Ar/³⁹Ar ages ranging from 14.2 to 11 Ma (MC36, MC420, MC422, MC423). We interpret the narrow staircase spectra between 10 and 14 Ma as mixed ages, reflecting the synkinematic neocrystallization of white micas over a time period of circa 4 Ma. Such an interpretation was already implied in interpreting similar spectra from the Helvetic Alps [Kirschner et al., 2003] and from the Aar massif in the Grimsel Pass area [Rolland et al., 2009]. The slight variation in Tschermak substitution in the phengites also argues for a variation in P-T-fluid conditions during synkinematic phengite growth [Guidotti, 1973]. The staircase spectra could thus be explained by the growth of phengite over circa 4 Ma, as retrograde P-T conditions gradually changed due to exhumation in the footwall of the SFZ. An alternative explanation could be that the phengite grew at around 14 Ma, and the younger steps are due to partial loss of ⁴⁰Ar [e.g., Simon-Labric et al., 2009]. This partial loss could be due to either (1) late reactivation or ongoing deformation reopening the system or (2) fluid percolation through the shear zones after or during deformation. In both cases, the synkinematic white mica would have an age of 14 Ma but with evidence for deformation and fluid circulation continuing until circa 10 Ma. A comparable two-point Rb/Sr age of 14.5 Ma was obtained from synkin-

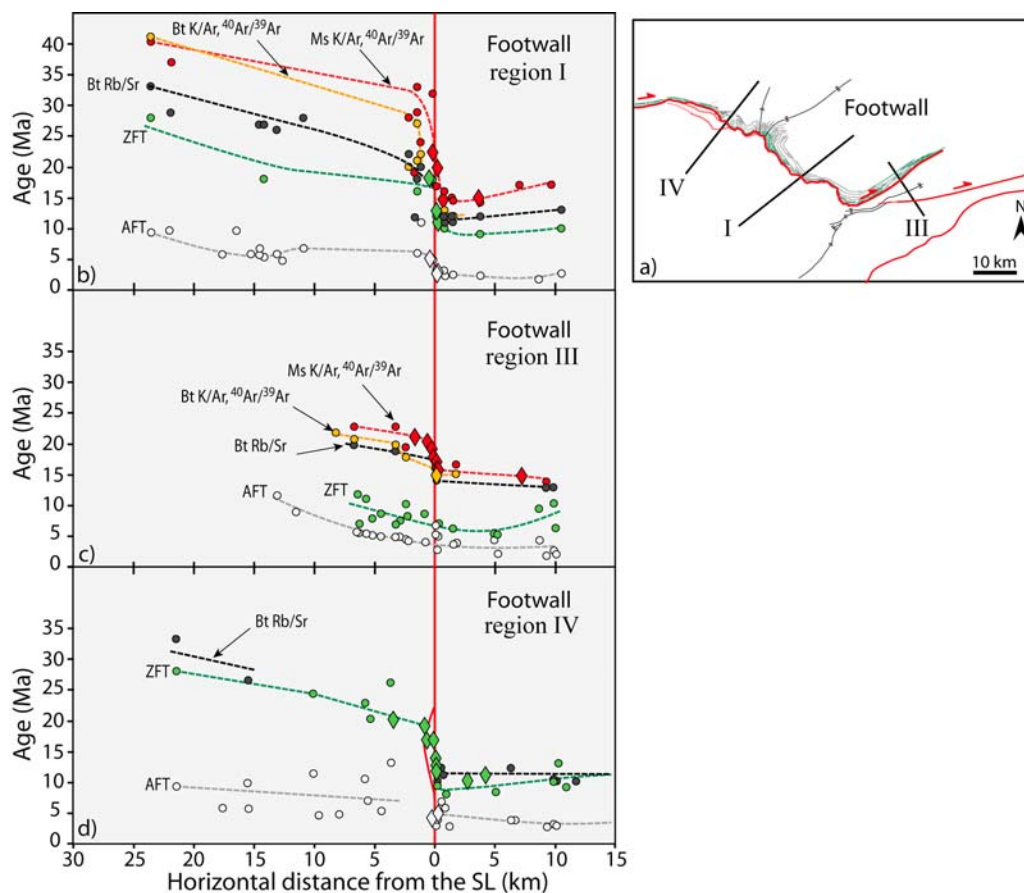


Figure 13. Cooling age patterns across the Simplon Fault Zone. (a) Location of three age-distance sections. (b) Age-distance section from the central region (region I). (c) Age-distance section from the SE region (region III). (d) Age-distance section from the NW region (region IV). These diagrams are a compilation of new cooling ages from this study (diamonds) and published data (circles) [Jäger *et al.*, 1967; Hunziker, 1969; Hunziker and Bearth, 1969; Purdy and Jäger, 1976; Wagner *et al.*, 1977; Deutsch and Steiger, 1985; Soom, 1990; Baxter *et al.*, 2002; Keller *et al.*, 2005a; Hetherington and Villa, 2007].

nematic phengite (MC 472) within the same phyllonite of the Aar massif (Figure 12d).

6.3. Dating Deformation Along the Simplon Fault Zone

[49] Crystallization ages obtained using $^{40}\text{Ar}/^{39}\text{Ar}$ and Rb/Sr geochronology throughout the Simplon region constrain the absolute age of Neogene deformation along the SFZ. The age of newly grown muscovite in veins developed in the necks of foliation boudins and Riedel fractures from the amphibolite facies Simplon mylonites (region III) suggests that in the SE the transition from ductile to brittle behavior during Simplon shearing occurred at 14–14.5 Ma. In the NW, ages of synkinematic phengite from a dextral strike slip phyllonite shear zone in the Rhone Valley (region V) brackets the time for the brittle-ductile transition of the Simplon-Rhone Line to be between 10 and 14.5 Ma, with continued shear deformation until circa 10 Ma. This continued shearing is younger than the ages of Simplon-Rhone Line activity proposed by Markley *et al.* [1998] (19 Ma) and Kirschner *et al.* [2003] (17 Ma).

6.4. Cooling Ages and Fault Activity

[50] The discontinuity in cooling ages (fission track and $^{40}\text{Ar}/^{39}\text{Ar}$) across the SFZ also provides constraints on the timing of fault activity. When plotted against horizontal distance from the SL, cooling ages for regions I, III and IV across the SL (Figure 13a) display the following features.

[51] 1. In the central part of the SFZ (region I), all different thermochronometers show a significant jump in cooling ages across the SFZ, consistent with a normal displacement as described by Steck and Hunziker [1994]. The distinctly different thermal histories from the hanging and footwall, for thermochronometers with a range of closure temperatures, argues for activity on the SFZ over a time period of at least 20 to 3 Ma (Figure 13b).

[52] 2. In the SE (region III), a slight jump in $^{40}\text{Ar}/^{39}\text{Ar}$ and Rb/Sr ages can be observed across the SFZ between 17 Ma and 14 Ma. This is attributed to a minor differential displacement between footwall and hanging wall, introduced by regional doming of the footwall during penetrative ductile shearing, as indicated by the variably plunging stretching

lineations (Figure 2c). However, no significant jump in cooling ages is seen for low-temperature fission track thermochronometers after 14 Ma (Figure 13c). As discussed above, this is attributed to late brittle dextral strike-slip movement on the SFZ postdating the regional up-doming of the footwall, which ceased at the time of the brittle transition around 14 Ma.

[53] 3. Finally in the NW (region IV), the different thermochronometers again show a significant overall jump in cooling ages across the SFZ, best preserved in the zircon fission track ages and consistent with a normal displacement (Figure 13d). Considering the general trend of apatite fission tracks ages, a slight jump in ages can still be distinguished between footwall and hanging wall. The younger ages observed within the footwall (14 to 4 Ma) are likely to reflect active displacement on the SFZ at this time, similar to the central part of the SFZ (region I). The jump observed in zircon fission track ages is spread over a wider zone compared to the central part of the SFZ (region I). This confirms that the brittle overprint in region IV is no longer localized on one discrete detachment and reflects the overall geometry of the detachment system at a higher structural level.

7. Conclusions

[54] The Simplon Fault Zone (SFZ) is a major extensional ductile shear zone with a subsequent brittle overprint, in part localized on a relatively discrete detachment, the “Simplon Line” (SL), that today separates the footwall and hanging wall. The kinematics for both ductile and brittle components is identical across and along the exposed length of the fault zone, from the Rhone Valley in the NW to the Isorno Valley in the SE. The regional pattern of cooling ages, with a significant jump across the detachment, argues for activity of the ductile shear zone since at least 20 Ma. The $^{40}\text{Ar}/^{39}\text{Ar}$ and Rb/Sr dating of synkinematic white micas from greenschist facies footwall phyllonite in the Rhone Valley yields ages of 14.5–10 Ma, whereas newly grown muscovite from veins in foliation boudinage necks in high grade mylonite in the Isorno Valley yield 14.5–14 Ma. Together these results bracket the ductile to brittle transition to the time interval between 14.5 and 10 Ma. Finally, fission track ages in combination with structural analyses strongly suggest that displacement along the entire fault zone has continued at lower temperature until circa 3–5 Ma. This argues for a continuous transition from ductile shearing to a more localized mode of brittle deformation within the same geological framework, over a period of circa 15 Ma during the Neogene. The SFZ is therefore an example of a telescoped crustal section in a major low-angle fault, developed during continued convergence, rather than a two-stage structure involving exhumation on a brittle fault of an earlier inactive ductile shear zone.

Appendix A: Fission Track Methodology

[55] The separation of zircon and apatite grains was achieved by conventional crushing, Wilfley table, magnetic and heavy liquid techniques [Seward, 1989]. Apatites and zircons were analyzed using the external detector method. Zircon grains were mounted in Teflon and polished. Samples were etched in NaOH-KOH eutectic melt at 210°C for 20–

23 h. Apatite grains were mounted on glass slides using epoxy glue and polished. Samples were etched in 7% HNO₃ for 50 s at 21°C. Irradiation was carried out at the ANSTO facility, Lucas Heights (Australia), and at the radiation center of Oregon State University, Corvallis (USA) with a nominal neutron flux of 1.0×10^{16} neutrons cm⁻² for apatite and 1.0×10^{15} neutrons cm⁻² for zircon. Mica detectors were etched after irradiation to reveal induced tracks using 40% HF at room temperature for 50 min. Microscopic analysis was carried out using a Zeiss Axioplan2 optical microscope with a computer-driven stage and FTstage 4 software from Dumitru [1993]. The magnification used was 1250x for apatite and 1600x (oil) for zircon. All ages were determined using the zeta approach [Hurford and Green, 1983] with a zeta value of 341 ± 6 for CN5/apatite, and of 130 ± 0.6 for CN1/zircon.

Appendix B: The $^{40}\text{Ar}/^{39}\text{Ar}$ Methodology

[56] Samples were crushed and washed in an ultrasonic bath for 10 min successively with water, alcohol and distilled water. Single grains of muscovite and biotite, and aggregates of phengite with a grain size between 800 and 200 μm were separated by hand-picking under a binocular microscope. Samples were irradiated in the nuclear reactor at McMaster University in Hamilton (Canada). The $^{40}\text{Ar}/^{39}\text{Ar}$ analysis was carried out by single-grain analysis with a 50 W SYNRAD CO₂ continuous laser. Isotopic ratios were measured using a VG3600 mass spectrometer, working with a Daly detector system, at the University of Nice (Géosciences Azur, France). The typical blank values for extraction and purification of the laser system are in the range 4.2–8.75, 1.2–3.9 cm³ STP for masses 40 and 39, respectively. Two samples MC22 and MC36 were analyzed in a step-heating experiment with a double-vacuum high-frequency furnace. Decay constants are those of Steiger and Jäger [1977] (5.543×10^{-10} y⁻¹). Isotopic measurements are corrected for isotopic interferences of K, Ca and Cl, mass discrimination and atmospheric argon contamination. Uncertainties on individual apparent ages are given at the 1σ level and do not include the error on the $^{40}\text{Ar}^*/^{39}\text{Ar}_k$ ratio of the monitor (±0.2%). Uncertainties on plateau ages and integrated ages are given at the 2σ level and do not include the error on the age of the monitor. A plateau age is defined when at least 70% of ³⁹Ar is released over a minimum of three successive steps. Using the laser on single grains has the advantage of avoiding mixed population ages but it produces a lower signal than with the furnace method. This is the reason why big mica flakes (800–200 μm) were chosen in this study and why, in some specific cases when the white micas were too small, a population of several individual grains was analyzed.

Appendix C: Rb/Sr Microsampling Methodology

[57] Microsampling was first carried out by cutting blocks parallel to the Simplon stretching lineation, from which polished thick sections ~50 μm thick were prepared using Crystalbond glue, which can be reheated and liquefied [cf. Müller et al., 2000a, 2000b]. White mica fibers growing

between broken porphyroclasts and calcite-white mica pairs in textural contact inside the veins were cut with a microscope-mounted microdrill. Microsamples were collected under a binocular microscope after heating the thick section. The samples were then cleaned in an ultrasonic bath for 10 min in successively acetone (x2), methanol, and IR-distilled water (x3), and subsequently weighed using a microbalance.

[58] The white micas were leached twice to ensure separation of silicates from residual carbonates with 250 μL of ~ 4 M acetic acid in an ultrasonic bath (10 min) and on a warm plate at 120°C (~ 2 h). After being rinsed with 200 μL of water, they were leached with 250 μL of 1M HCl on a warm plate at 120°C for ~ 5 min. Subsequently, the samples were rinsed with 300 μL of water and weighed afterward to calculate mass and density. After addition of a mixed ^{84}Sr - ^{85}Rb tracer solution, the silicate samples were then dissolved in closed Teflon vials at 120°C with 600 μL HF and 30 μL HNO_3 for about 2–3 days. After evaporation, samples were equilibrated overnight with 600 μL 6M HCl at 120°C, followed with 10 min in the ultrasonic bath. Calcite samples were dissolved in closed Teflon vials at 120°C with 400 μL of 1 M HCl for about 1 day after addition of a ^{84}Sr - ^{85}Rb tracer. Rb and Sr were purified using microcolumns of 0.377 mL of cation resin as a first step, and the broad Sr cut was further purified using a 50 μL SrSpec column.

[59] Isotopic analyses were carried out using thermal ionization mass spectrometry (TIMS), on a Thermo-Finnigan Triton mass spectrometer (Open University, United Kingdom) for Sr and a VG354 at Royal Holloway University of London for Rb, in both cases using a Ta-emitter solution on zone-refined outgassed Re filaments [Birck, 1986]. Sr blanks were 31.6 and 40 pg and no blank correction was necessary;

repeated analysis of SRM987 yielded 0.710280 ± 0.000010 (2 SD). Constants were those from Steiger and Jäger [1977].

Appendix D: Oxygen Isotope Methodology

[60] Quartz and white mica in textural contact inside each vein where isolated by cutting with a millimeter thick saw and crushed. Final mineral separates were carefully chosen under a binocular microscope to avoid inclusions. Oxygen isotopes were measured at the University of Lausanne. Analyses were made on 0.5 to 2 mg of sample material. Samples were loaded onto a small Pt sample holder and pumped to a vacuum of about 10^{-6} mbar. After pre-flourination of the sample chamber overnight, the samples were heated with an infrared CO_2 laser in 50 mbar of pure F_2 . Excess F_2 is separated from the O_2 produced by conversion to Cl_2 using KCl held at 150°C. The extracted O_2 is collected on a molecular sieve and subsequently expanded into the inlet of a Finnigan MAT 253 isotope ratio mass spectrometer. Oxygen isotope compositions are given in the standard δ notation, expressed relative to VSMOW in permil (‰). Replicate oxygen isotope analyses of the standards used (NBS-28 quartz, four replicates for each day of analysis) generally have an average precision of $\pm 0.1\text{‰}$ for $\delta^{18}\text{O}$. The accuracy of $\delta^{18}\text{O}$ values is commonly better than 0.2‰ compared to accepted $\delta^{18}\text{O}$ values for NBS28 of 9.64‰.

[61] **Acknowledgments.** We would like to thank Michele Sapigni from Enel Power for providing us core samples from the Baceno schist. We also thank Michael Wiederkehr and an anonymous reviewer for their comments and suggestions. This work was financed by the Swiss National Foundation, projects: NF 200021-109187 and NF 200020-121578.

References

- Armstrong, R. L., E. Jäger, and P. Eberhardt (1966), A comparison of K/Ar and Rb/Sr ages on Alpine biotites, *Earth Planet. Sci. Lett.*, *1*, 13–19, doi:10.1016/0012-821X(66)90097-5.
- Arslan, A., C. W. Passchier, and D. Koehn (2008), Foliation boudinage, *J. Struct. Geol.*, *30*, 291–309, doi:10.1016/j.jsg.2007.11.004.
- Axen, G. J., and J. M. Bartley (1997), Field tests of rolling hinges: Existence, mechanical types, and implications for extensional tectonics, *J. Geophys. Res.*, *102*, 20,515–20,537, doi:10.1029/97JB01355.
- Baxter, E. F., D. J. DePaolo, and P. R. Renne (2002), Spatially correlated anomalous $^{40}\text{Ar}/^{39}\text{Ar}$ “age” variations in biotites about a lithologic contact near Simplon Pass, Switzerland: A mechanistic explanation for excess Ar, *Geochim. Cosmochim. Acta*, *66*, 1067–1083, doi:10.1016/S0016-7037(01)00828-6.
- Bearth, P. (1956a), Zur Geologie der Wurzelzone östlich des Ossolatales, *Eclogae Geol. Helv.*, *49*, 267–278.
- Bearth, P. (1956b), Geologische Beobachtungen im Grenzgebiet der Lepontinischen und Penninischen Alpen, *Eclogae Geol. Helv.*, *49*, 279–290.
- Bearth, P. (1958), Ueber einen Wechsel der Mineralfazies in der Wurzelzone des Penninikums, *Schweiz. Mineral. Petrogr. Mitt.*, *38*, 363–373.
- Behrmann, J. H. (1988), Crustal-scale extension in a convergent orogen: The Sterzing-Steinach mylonite zone in the Eastern Alps, *Geodin. Acta*, *2*, 63–73.
- Berthé, D., P. Choukroune, and P. Jegouzo (1979), Orthogneiss, mylonite and non coaxial deformation of granites: Example of the South Armorican shear zone, *J. Struct. Geol.*, *1*, 31–42, doi:10.1016/0191-8141(79)90019-1.
- Birck, J. L. (1986), Precision K-Rb-Sr isotopic analysis: Application to Rb-Sr chronology, *Chem. Geol.*, *56*, 73–83, doi:10.1016/0009-2541(86)90111-7.
- Bousquet, R., R. Oberhänsli, B. Goffé, M. Wiederkehr, F. Koller, S. M. Schmid, R. Schuster, M. Engi, A. Berger, and G. Martinotti (2008), Metamorphism of metasediments at the scale of an orogen: A key to the Tertiary geodynamic evolution of the Alps, in *Tectonic Aspects of the Alpine-Dinaride-Carpathian System*, edited by S. Siegesmund et al., *Geol. Soc. Spec. Publ.*, *298*, 393–411, doi:10.1144/SP298.18.
- Brichau, S., U. Ring, R. A. Ketcham, A. Carter, D. Stockli, and M. Brunel (2006), Constraining the long-term evolution of the slip rate for a major extensional fault system in the central Aegean, Greece, using thermochronology, *Earth Planet. Sci. Lett.*, *241*, 293–306, doi:10.1016/j.epsl.2005.09.065.
- Burkhard, M. (1988), L’Helvétique de la bordure occidentale du massif de l’Aar (évolution tectonique et métamorphique), *Eclogae Geol. Helv.*, *81*, 63–114.
- Campani, M. (2009), Temporal and spatial evolution of a syn-orogenic extensional system: The Simplon Fault Zone, Ph.D. thesis, ETH Zurich, Zurich, Switzerland.
- Chacko, T., X. S. Hu, T. K. Mayeda, R. N. Clayton, and J. R. Goldsmith (1996), Oxygen isotope fractionations in muscovite, phlogopite, and rutile, *Geochim. Cosmochim. Acta*, *60*, 2595–2608, doi:10.1016/0016-7037(96)00112-3.
- Challandes, N., D. Marquer, and I. M. Villa (2003), Dating the evolution of C-S microstructures: A combined $^{40}\text{Ar}/^{39}\text{Ar}$ step-heating and UV laserprobe analysis of the Alpine Rofna shear zone, *Chem. Geol.*, *197*, 3–19, doi:10.1016/S0009-2541(02)00354-6.
- Challandes, N., D. Marquer, and I. M. Villa (2008), P-T-t modelling, fluid circulation, and ^{39}Ar - ^{40}Ar and Rb-Sr mica ages in the Aar Massif shear zones (Swiss Alps), *Swiss J. Geosci.*, *101*, 269–288, doi:10.1007/s00015-008-1260-6.
- Chopin, C., and P. Monié (1984), A unique magnesiochloritoid-bearing, high-pressure assemblage from the Monte Rosa, Western Alps: Petrologic and ^{40}Ar - ^{39}Ar radiometric study, *Contrib. Mineral. Petrol.*, *87*, 388–398, doi:10.1007/BF00381295.
- Davis, G. A. (1988), Rapid upward transport of mid-crustal mylonitic gneisses in the footwall of a Miocene detachment fault, Whipple Mountains, southeastern California, *Geol. Rundsch.*, *77*, 191–209, doi:10.1007/BF01848684.
- Deutsch, A., and R. H. Steiger (1985), Hornblende K-Ar ages and the climax of Tertiary metamorphism in the Lepontine Alps (south-central Switzerland): An old problem reassessed, *Earth Planet. Sci. Lett.*, *72*, 175–189, doi:10.1016/0012-821X(85)90004-4.
- Dodson, M. H. (1973), Closure temperature in cooling geochronological and petrological systems, *Contrib. Mineral. Petrol.*, *40*, 259–274, doi:10.1007/BF00373790.
- Dumitru, T. A. (1993), A new computer automated microscope stage system for fission track analysis,

- Nucl. Tracks Radiat. Meas.*, 21, 575–580, doi:10.1016/1359-0189(93)90198-1.
- Dunlap, W. J. (1997), Neocrystallization or cooling? $^{40}\text{Ar}/^{39}\text{Ar}$ ages of white micas from low-grade mylonites, *Chem. Geol.*, 143, 181–203, doi:10.1016/S0009-2541(97)00113-7.
- Engi, M., R. Bousquet, and A. Berger (2004), Metamorphic structure of the central Alps, in Explanatory notes to the map “Metamorphic structure of the Alps, *Mitt. Oesterr. Geol. Ges.*, 149, 157–173.
- Foster, D. A., A. J. W. Gleadow, S. J. Reynolds, and P. G. Fitzgerald (1993), Denudation of metamorphic core complexes and the reconstruction of the transition zone, west central Arizona: Constraints from apatite fission track thermochronology, *J. Geophys. Res.*, 98, 2167–2185, doi:10.1029/92JB02407.
- Frank, E. (1983), Alpine metamorphism of calcareous rocks along a cross-section in the central Alps: Occurrence and breakdown of muscovite, margarite and paragonite, *Schweiz. Mineral. Petrogr. Mitt.*, 63, 37–93.
- Frank, E., and A. Stettler (1979), K-Ar and ^{39}Ar - ^{40}Ar systematics of white K-mica from an Alpine metamorphic profile in the Swiss Alps, *Schweiz. Mineral. Petrogr. Mitt.*, 59, 375–394.
- Frey, M., and R. Ferreiro Mählmann (1999), Alpine metamorphism of the central Alps, *Schweiz. Mineral. Petrogr. Mitt.*, 79, 135–154.
- Frey, M., J. Hunziker, W. Frank, J. Bocquet, G. V. Dal Piaz, E. Jäger, and E. Niggli (1974), Alpine metamorphism of the Alps: A review, *Schweiz. Mineral. Petrogr. Mitt.*, 54, 247–290.
- Fügenschuh, B., D. Seward, and N. Mancktelow (1997), Exhumation in a convergent orogen: The western Tauern window, *Terra Nova*, 9, 213–217, doi:10.1046/j.1365-3121.1997.d01-33.x.
- Galbraith, R. F. (1981), On statistical-models for fission-track counts, *J. Int. Assoc. Math. Geol.*, 13, 471–478, doi:10.1007/BF01034498.
- Grasemann, B., and N. S. Mancktelow (1993), Two-dimensional thermal modeling of normal faulting: The Simplon Fault Zone, central Alps, Switzerland, *Tectonophysics*, 225, 155–165, doi:10.1016/0040-1951(93)90277-Q.
- Grosjean, G., C. Sue, and M. Burkhard (2004), Late Neogene extension in the vicinity of the Simplon Fault Zone (central Alps, Switzerland), *Ecolgæ Geol. Helv.*, 97, 33–46, doi:10.1007/s00015-004-1114-9.
- Grujic, D., and N. S. Mancktelow (1996), Structure of the northern Maggia and Lebendun nappes, central Alps, Switzerland, *Ecolgæ Geol. Helv.*, 89, 461–504.
- Guidotti, C. V. (1973), Compositional variation of muscovite as a function of metamorphic grade and assemblages in metapelites from N.W. Maine, *Contrib. Mineral. Petrol.*, 42, 33–42.
- Hames, W. E., and S. A. Bowring (1994), An empirical evaluation of the argon diffusion geometry in muscovite, *Earth Planet. Sci. Lett.*, 124, 161–167, doi:10.1016/0012-821X(94)00079-4.
- Harrison, T. M., J. Celerier, A. B. Aikman, J. Hermann, and M. T. Heizler (2009), Diffusion of ^{40}Ar in muscovite, *Geochim. Cosmochim. Acta*, 73, 1039–1051, doi:10.1016/j.gca.2008.09.038.
- Heinrich, C. A. (1986), Eclogite facies regional metamorphism of hydrous mafic rocks in the central Alpine Adula nappe, *J. Petrol.*, 27, 123–154.
- Hetherington, C. J., and I. M. Villa (2007), Barium silicates of the Berisal complex, Switzerland: A study in geochronology and rare-gas release systematics, *Geochim. Cosmochim. Acta*, 71, 3336–3347, doi:10.1016/j.gca.2007.05.001.
- Hunziker, J. (1969), Rb-Sr Altersbestimmungen aus den Walliser Alpen, Hellglimmer- und Gesamtgesteinsalterswerte, *Ecolgæ Geol. Helv.*, 62, 527–542.
- Hunziker, J., and P. Bearth (1969), Rb-Sr Altersbestimmungen aus den Walliser-Alpen: Biotitalterswerte und ihre Bedeutung für die Abkühlungsgeschichte der alpinen Metamorphose, *Ecolgæ Geol. Helv.*, 62, 205–222.
- Hurford, A. J., and P. F. Green (1983), The zeta-age calibration of fission-track dating, *Isot. Geosci.*, 1, 285–317.
- Jäger, E. (1965), Rb/Sr age determination on minerals and rocks from the Alps, *Sci. Terre*, 10, 395–406.
- Jäger, E., E. Niggli, and E. Wenk (1967), Rb-Sr Altersbestimmungen an Glimmern der Zentralalpen, *Beitr. Geol. Karte Schweiz*, 134.
- Keller, L. M., R. Abart, S. M. Schmid, and C. De Capitani (2005a), Phase relations and chemical composition of phengite and paragonite in pelitic schists during decompression: A case study from the Monte Rosa nappe and Camughera-Moncucco unit, Western Alps, *J. Petrol.*, 46, 2145–2166, doi:10.1093/ptrology/egi051.
- Keller, L. M., M. Hess, B. Fügenschuh, and S. M. Schmid (2005b), Structural and metamorphic evolution of the Camughera-Moncucco, Antrona and Monte Rosa units southwest of the Simplon Line, Western Alps, *Ecolgæ Geol. Helv.*, 98, 19–49, doi:10.1007/s00015-005-1149-6.
- Keller, L. M., B. Fügenschuh, M. Hess, B. Schneider, and S. M. Schmid (2006), Simplon Fault Zone in the Western and central Alps: Mechanism of Neogene faulting and folding revisited, *Geology*, 34, 317–320, doi:10.1130/G22256.1.
- Kirschner, D. L., H. Masson, and M. A. Cosca (2003), An $^{40}\text{Ar}/^{39}\text{Ar}$, Rb/Sr, and stable isotope study of micas in low-grade fold-and-thrust belt: An example from the Swiss Helvetic Alps, *Contrib. Mineral. Petrol.*, 145, 460–480, doi:10.1007/s00410-003-0461-2.
- Kretz, R. (1983), Symbols for rock-forming minerals, *Am. Mineral.*, 68, 277–279.
- Lacassin, R. (1988), Large-scale foliation boudinage in gneisses, *J. Struct. Geol.*, 10, 643–647, doi:10.1016/0191-8141(88)90030-2.
- Lardeaux, J. M., G. Gosso, J. R. Kienast, and B. Lombardo (1982), Metamorphism and deformation in Sesia-Lanzo site (Western Alps) and eclogitization of continental-crust, *Bull. Soc. Geol. Fr.*, 24, 793–800.
- Laubscher, H. P. (1971), The large-scale kinematics of the western Alps and the northern Apennines and its palinspastic implications, *Am. J. Sci.*, 271, 193–226.
- Lister, G. S., and G. A. Davis (1989), The origin of metamorphic core complexes and detachment faults formed during Tertiary continental extension in the northern Colorado river region, USA, *J. Struct. Geol.*, 11, 65–94, doi:10.1016/0191-8141(89)90036-9.
- Mancel, P., and O. Merle (1987), Kinematics of the northern part of the Simplon Line (central Alps), *Tectonophysics*, 135, 265–275, doi:10.1016/0040-1951(87)90111-9.
- Mancktelow, N. (1985), The Simplon Line: A major displacement zone in the Western Lepontine Alps, *Ecolgæ Geol. Helv.*, 78, 73–96.
- Mancktelow, N. S. (1987), Quartz textures from the Simplon Fault Zone, southwest Switzerland and north Italy, *Tectonophysics*, 135, 133–153, doi:10.1016/0040-1951(87)90157-0.
- Mancktelow, N. (1990), *The Simplon Fault Zone*, *Beitr. Geol. Karte Schweiz*, 163, 74 pp.
- Mancktelow, N. S. (1992), Neogene lateral extension during convergence in the central Alps: Evidence from interrelated faulting and backfolding around the Simplon pass (Switzerland), *Tectonophysics*, 215, 295–317, doi:10.1016/0040-1951(92)90358-D.
- Mancktelow, N. S., and T. L. Pavlis (1994), Fold-fault relationships in low-angle detachment systems, *Tectonics*, 13, 668–685, doi:10.1029/93TC03489.
- Markley, M. J., C. Teysier, M. A. Cosca, R. Caby, J. C. Hunziker, and M. Sartori (1998), Alpine deformation and $^{40}\text{Ar}/^{39}\text{Ar}$ geochronology of synkinematic white mica in the Siviez-Mischabel nappe, Western Pennine Alps, Switzerland, *Tectonics*, 17, 407–425, doi:10.1029/98TC000560.
- Maxelon, M., and N. S. Mancktelow (2005), Three-dimensional geometry and tectonostratigraphy of the Pennine zone, central Alps, Switzerland and northern Italy, *Earth Sci. Rev.*, 71, 171–227, doi:10.1016/j.earscirev.2005.01.003.
- Mehl, C., L. Jolivet, and O. Lacombe (2005), From ductile to brittle: Evolution and localization of deformation below a crustal detachment (Tinos, Cyclades, Greece), *Tectonics*, 24, TC4017, doi:10.1029/2004TC001767.
- Merle, O. (1987), Deformation history in the western Lepontine Alps, *Bull. Soc. Geol. Fr.*, 3, 183–190.
- Merle, O., P. Legal, and P. Mancel (1986), Déformation et métamorphisme dans la région du Simplon (Alpes centrales), *Ecolgæ Geol. Helv.*, 79, 705–718.
- Michalski, I., and M. A. Soom (1990), The Alpine thermo-tectonic evolution of the Aar and Gotthard massifs, central Switzerland: Fission track ages on zircon and apatite and K-Ar mica ages, *Schweiz. Mineral. Petrogr. Mitt.*, 70, 373–387.
- Milnes, A. G. (1974), Structure of the Pennine zone (central Alps): A new working hypothesis, *Geol. Soc. Am. Bull.*, 85, 1727–1732, doi:10.1130/0016-7606(1974)85<1727:SOTPZC>2.0.CO;2.
- Milnes, A. G., M. Grellier, and R. Müller (1981), Sequence and style of major post-nappe structures, Simplon-Pennine Alps, *J. Struct. Geol.*, 3, 411–420, doi:10.1016/0191-8141(81)90041-9.
- Mulch, A., and M. A. Cosca (2004), Recrystallization or cooling ages: In situ UV-laser $^{40}\text{Ar}/^{39}\text{Ar}$ geochronology of muscovite in mylonitic rocks, *J. Geol. Soc.*, 161, 573–582, doi:10.1144/0016-764903-110.
- Mulch, A., M. A. Cosca, A. Andresen, and J. Fiebig (2005), Time scales of deformation and exhumation in extensional detachment systems determined by high-spatial resolution in situ UV-laser $^{40}\text{Ar}/^{39}\text{Ar}$ dating, *Earth Planet. Sci. Lett.*, 233, 375–390, doi:10.1016/j.epsl.2005.01.042.
- Mulch, A., C. Teysier, M. A. Cosca, and T. W. Vennemann (2006), Thermomechanical analysis of strain localization in a ductile detachment zone, *J. Geophys. Res.*, 111, B12405, doi:10.1029/2005JB004032.
- Müller, W., D. Aerden, and A. N. Halliday (2000a), Isotopic dating of strain fringe increments: Duration and rates of deformation in shear zones, *Science*, 288, 2195–2198, doi:10.1126/science.288.5474.2195.
- Müller, W., N. S. Mancktelow, and M. Meir (2000b), Rb-Sr microchrons of synkinematic mica in mylonites: An example from the DAV fault of the Eastern Alps, *Earth Planet. Sci. Lett.*, 180, 385–397, doi:10.1016/S0012-821X(00)00167-9.
- Niggli, C. (1970), Alpine metamorphose und alpine Gebirgsbildung, *Fortschr. Mineral.*, 47, 16–26.
- Niggli, E., and C. Niggli (1965), Karten der Verbreitung einiger Mineralien der alpidischen Metamorphose in den schweizer Alpen (Stilpnomelan, Alkali-Amphibol, Chloritoid, Staurolith, Disthen, Sillimanit), *Ecolgæ Geol. Helv.*, 58, 335–368.
- Passchier, C. W. (2001), Flanking structures, *J. Struct. Geol.*, 23, 951–962, doi:10.1016/S0191-8141(00)00166-8.
- Pettke, T., L. W. Diamond, and I. M. Villa (1999), Mesothermal gold veins and metamorphic devolatilization in the northwestern Alps: The temporal link, *Geology*, 27, 641–644, doi:10.1130/0091-7613(1999)027<0641:MGVAMD>2.3.CO;2.
- Preiswerk, H. (1921), Die zwei Querckenulminationen Tosa-Tessin und die Tessiner Deckerfalte, *Ecolgæ Geol. Helv.*, 16, 485–496.
- Purdy, J. W., and E. Jäger (1976), K-Ar ages on rock-forming minerals from the central Alps, *Mem. Ist. Geol. Mineral. Univ. Padova*, 30, 1–31.
- Purdy, J. W., and H. A. Stalder (1973), K-Ar ages of fissure minerals from the Swiss Alps, *Schweiz. Mineral. Petrogr. Mitt.*, 53, 79–98.
- Reinecke, T. (1991), Very-high-pressure metamorphism and uplift of coesite-bearing metasediments from the Zermatt-Saas zone, Western Alps, *Eur. J. Mineral.*, 3, 7–17.
- Rieder, M., et al. (1998), Nomenclature of the micas, *Can. Mineral.*, 36, 905–912.
- Rolland, Y., M. Rossi, S. F. Cox, M. Corsini, N. Mancktelow, G. Pennacchioni, M. Fornari, and A. M. Boullier (2008), $^{40}\text{Ar}/^{39}\text{Ar}$ dating of synkinematic white mica: Insights from fluid-rock reaction

- in low-grade shear zones (Mont Blanc Massif) and constraints on timing of deformation in the NW external Alps, in *The Internal Structure of Fault Zones: Implications for Mechanical and Fluid-Flow Properties*, edited by C. A. J. Wibberley et al., *Geol. Soc. Spec. Publ.*, 299, 293–315, doi:10.1144/SP299.18.
- Rolland, Y., S. F. Cox, and M. Corsini (2009), Constraining deformation stages in brittle-ductile shear zones from combined field mapping and $^{40}\text{Ar}/^{39}\text{Ar}$ dating: The structural evolution of the Grimsel Pass area (Aar Massif, Swiss Alps), *J. Struct. Geol.*, 31, 1377–1394, doi:10.1016/j.jsg.2009.08.003.
- Romer, R. L., U. Schärer, and A. Steck (1996), Alpine and pre-Alpine magmatism in the root-zone of the western central Alps, *Contrib. Mineral. Petrol.*, 123, 138–158, doi:10.1007/s004100050147.
- Rossi, M., Y. Rolland, O. Vidal, and S. F. Cox (2005), Geochemical variations and element transfer during shear-zone development and related episyenites at middle crust depths: Insights from the Mont Blanc granite (French-Italian Alps), in *High-Strain Zones: Structure and Physical Properties*, edited by D. Bruhn and L. Burlini, *Geol. Soc. Spec. Publ.*, 245, 373–396, doi:10.1144/GSL.SP.2005.245.01.18.
- Schmid, S. M., and E. Kissling (2000), The arc of the Western Alps in the light of geophysical data on deep crustal structure, *Tectonics*, 19, 62–85, doi:10.1029/1999TC900057.
- Schmid, S. M., B. Fügenschuh, E. Kissling, and R. Schuster (2004), Tectonic map and overall architecture of the Alpine orogen, *Ecolgae Geol. Helv.*, 97, 93–117, doi:10.1007/s00015-004-1113-x.
- Selverstone, J. (1988), Evidence for east-west crustal extension in the Eastern Alps: Implications for the unroofing history of the Tauern window, *Tectonics*, 7, 87–105, doi:10.1029/TC007i001p0087.
- Seward, D. (1989), Cenozoic basin histories determined by fission-track dating of basement granites, South Island, New-Zealand, *Chem. Geol.*, 79, 31–48.
- Seward, D., and N. S. Mancktelow (1994), Neogene kinematics of the central and Western Alps: Evidence from fission-track dating, *Geology*, 22, 803–806, doi:10.1130/0091-7613(1994)022<0803: NKOTCA>2.3.CO;2.
- Sibson, R. H. (1983), Continental fault structure and the shallow earthquake source, *J. Geol. Soc.*, 140, 741–767, doi:10.1144/gsjgs.140.5.0741.
- Simon-Labric, T., Y. Rolland, T. Dumont, T. Heymes, C. Authemayou, M. Corsini, and M. Fornari (2009), $^{40}\text{Ar}/^{39}\text{Ar}$ dating of Penninic front tectonic displacement (W Alps) during the lower Oligocene (31–34 Ma), *Terra Nova*, 21, 127–136, doi:10.1111/j.1365-3121.2009.00865.x.
- Soom, M. A. (1990), Abkühlungs- und Hebungsgeschichte der Externmassive und der penninischen Decken beidseits der Simplon-Rhone-Linie seit dem Oligozän: Spaltspurdaterungen an Apatit/Zirkon und K-Ar-Datierungen an Biotit/Muskowit (westliche Zentralalpen), Ph.D. thesis, Univ. Bern, Bern.
- Steck, A. (1984), Tertiary deformation structures in the central Alps, *Ecolgae Geol. Helv.*, 77, 55–100.
- Steck, A. (1987), Le massif du Simplon—Réflexions sur la cinématique des nappes de gneiss, *Schweiz. Mineral. Petrogr. Mitt.*, 67, 27–45.
- Steck, A. (1990), A map of ductile shear zones of the central Alps, *Ecolgae Geol. Helv.*, 83, 603–627.
- Steck, A. (2008), Tectonics of the Simplon massif and Lepontine gneiss dome: Deformation structures due to collision between the underthrusting European plate and the Adriatic indenter, *Swiss. J. Geosci. Prague*, 101, 515–546.
- Steck, A., and J. Hunziker (1994), The Tertiary structural and thermal evolution of the central Alps—Compressional and extensional structures in an orogenic belt, *Tectonophysics*, 238, 229–254, doi:10.1016/0040-1951(94)90058-2.
- Steiger, R. H., and E. Jäger (1977), Subcommittee on geochronology: Convention on use of decay constants in geochronology and cosmochronology, *Earth Planet. Sci. Lett.*, 36, 359–362, doi:10.1016/0012-821X(77)90060-7.
- Todd, C. S., and M. Engi (1997), Metamorphic field gradients in the central Alps, *J. Metamorph. Geol.*, 15, 513–530, doi:10.1111/j.1525-1314.1997.00038.x.
- Trommsdorff, V. (1966), Progressive Metamorphose kieseliges Karbonatgesteine in den Zentralalpen zwischen Bernina und Simplon, *Schweiz. Mineral. Petrogr. Mitt.*, 46, 431–460.
- Trommsdorff, V. (1972), Change in T-X during metamorphism of siliceous dolomite rocks of the central Alps, *Schweiz. Mineral. Petrogr. Mitt.*, 52, 567–571.
- Vance, D., and R. K. O’Nions (1992), Prograde and retrograde thermal histories from the central Swiss Alps, *Earth Planet. Sci. Lett.*, 114, 113–129, doi:10.1016/0012-821X(92)90155-O.
- Vanderhaeghe, O., C. Teyssier, I. McDougall, and W. J. Dunlap (2003), Cooling and exhumation of the Shuswap metamorphic core complex constrained by $^{40}\text{Ar}/^{39}\text{Ar}$ thermochronology, *Geol. Soc. Am. Bull.*, 115, 200–216, doi:10.1130/0016-7606(2003)115<0200:CAEOTS>2.0.CO;2.
- Vernon, A. J., P. A. van der Beek, H. D. Sinclair, and M. K. Rahn (2008), Increase in late Neogene denudation of the European Alps confirmed by analysis of a fission-track thermochronology database, *Earth Planet. Sci. Lett.*, 270, 316–329, doi:10.1016/j.epsl.2008.03.053.
- Villa, I. M. (1998), Isotopic closure, *Terra Nova*, 10, 42–47, doi:10.1046/j.1365-3121.1998.00156.x.
- Wagner, G. A., G. M. Reimer, and E. Jäger (1977), Cooling ages derived by apatite fission-track, mica Rb-Sr and K-Ar dating: The uplift and cooling history of the central Alps, *Mem. Ist. Geol. Mineral. Univ. Padova*, 30, 1–27.
- Wells, M. L., L. W. Snee, and A. E. Blythe (2000), Dating of major normal fault systems using thermochronology: An example from the Raft River detachment, Basin and Range, western United States, *J. Geophys. Res.*, 105, 16,303–16,327, doi:10.1029/2000JB900094.
- Wenk, E. (1955), Eine Strukturkarte der Tessiner Alpen, *Schweiz. Mineral. Petrogr. Mitt.*, 53, 311–319.
- Wenk, E., and H. R. Wenk (1984), Distribution of plagioclase in carbonate rocks from the Tertiary metamorphic belt of the central Alps, *Bull. Mineral.*, 107, 357–368.
- Wiederkehr, M., R. Bousquet, S. M. Schmid, and A. Berger (2008), From subduction to collision: Thermal overprint of HP/LT meta-sediments in the north-eastern Lepontine Dome (Swiss Alps) and consequences regarding the tectono-metamorphic evolution of the Alpine orogenic wedge, *Swiss J. Geosci.*, 101, suppl. 1, 127–155, doi:10.1007/s00015-008-1289-6.
- Zwingmann, H., and N. Mancktelow (2004), Timing of Alpine fault gouges, *Earth Planet. Sci. Lett.*, 223, 415–425, doi:10.1016/j.epsl.2004.04.041.

M. Campani, Institut für Geologie, Leibniz Universität Hannover, Callinstrasse 30, D-30167 Hannover, Germany. (campani@geowi.uni-hannover.de)

I. Guerra, IMG, Quartier UNIL-Dorigny, Bat. Anthropole 4168, CH-1015 Lausanne, Switzerland.

N. Mancktelow and D. Seward, Department of Earth Sciences, ETH Zürich, CH-8092 Zürich, Switzerland.

W. Müller, Department of Earth Sciences, Royal Holloway, University of London, Egham TW20 0EX, UK.

Y. Rolland, Géosciences Azur, Université de Nice Sophia Antipolis, CNRS, IRD, 28 Av. de Valrose, BP 2135, F-06103 Nice, France. (yrolland@unice.fr)